이학박사 학위논문

# Proton Beam Irradiation Effect on Nanomaterials: $WSe_2$ and $MAPbI_3$

고에너지 양성자 조사가 나노 물질(이차원 텅스텐 다이셀레나이드와 메틸암모늄 납 할라이드 페로브스카이트)에 미치는 영향

2022 년 8 월

서울대학교 대학원

물리·천문학부

신 지 원

# Proton Beam Irradiation Effect on Nanomaterials: $WSe_2$ and $MAPbI_3$

고에너지 양성자 조사가 나노 물질(이차원 텅스텐 다이셀레나이드와 메틸암모늄 납 할라이드 페로브스카이트)에 미치는 영향

지도 교수 이 탁 희

이 논문을 이학박사 학위논문으로 제출함
2022 년 8 월

서울대학교 대학원
물리·천문학부 물리학 전공
신 지 원

신지원의 이학박사 학위논문을 인준함
2022 년 8 월

| | | |
|---|---|---|
| 위 원 장 | 차 국 린 | (인) |
| 부위원장 | 이 탁 희 | (인) |
| 위 원 | 민 홍 기 | (인) |
| 위 원 | 이 지 은 | (인) |
| 위 원 | 조 경 준 | (인) |

# Abstract

# Proton Beam Irradiation Effect on Nanomaterials: $WSe_2$ and $MAPbI_3$

**Jiwon Shin**

Department of Physics and Astronomy

Seoul National University

The study of the effect of proton beam irradiation on electronic devices such as transistors and solar cells has several advantages. The first is that the electrical or optical performance of a device can be controlled. A high-energy proton beam can be used to induce defects in the device to control the electrical characteristics such as current level, and a low-energy proton beam can be used to exfoliate the layered material into a monolayer to significantly improve its optical properties. However, further studies are needed to elucidate the mechanism of this phenomenon. The second is that it is possible to explore the potential of using the electronic devices in high-radiation environments such as space. Especially, research of the proton irradiation effect is important in terms of space application because protons occupy a high proportion among various elements of cosmic ray such as gamma rays, electrons, and neutrons. Organic-inorganic lead halide

perovskite, one of the materials I researched, is attracting attention as a next-generation solar cell material due to its high power conversion efficiency. Also, it has high potential for the space industry because of its high radiation hardness. Due to these advantages, it is being actively studied, but more research is needed to take full advantage of their stability and performance under radiation conditions.

In this manner, first I fabricated $WSe_2$ (one of transition metal chalcogenide) ambipolar field effect transistors and investigated the proton irradiation effect. Transition metal chalcogenide is a two-dimensional material attracting attention as a next-generation device material because of its remarkable electrical and optical properties such as high mobility and high photosensitivity. Among them, $WSe_2$ has a unique property that the carrier type of the electronic device varies depending on the thickness; p-type for thin thickness, ambipolar for intermediate thickness, and n-type for thick. Here, an ambipolar type transistor was designed and fabricated to examine the proton effect on both the electron accumulation region and the hole accumulation region. The electrical and physicochemical properties of the devices were measured and systematically compared before and after the high energy proton beam irradiation of 10 MeV under various dose conditions. The physicochemical properties did not change within the measurement limits. However, the electrical characteristics such as current level and threshold voltages were changed after the irradiation and the amount (and direction) of change were affected by the dose. These changes were explained by the proton irradiation-induced traps referred to herein as “positive bulk traps” and “negative interface traps”.

Secondly, I synthesized organic-inorganic lead halide perovskite by two different methods, mechanochemical synthesis and flash evaporation, and

investigated the proton irradiation hardness of the synthesized perovskite. Since both methods are dry synthesis methods, they have the advantage of being less toxic than the spin coating method, which is one of the representative perovskite synthesis methods. The synthesized materials were exposed to high-energy proton beams under various irradiation doses and physicochemical properties of the materials were compared before and after the proton irradiation. The properties of mechanochemically synthesized perovskite did not change noticeably even under high irradiation doses, whereas the properties of flash-evaporated perovskite did. This difference was explained by the stronger bonding energy due to its less defects in mechanochemically synthesized perovskite.

주요어 : Proton irradiation, Nanomaterial, Transition metal dichalcogenide, Tungsten diselenide, Organic-inorganic perovskite, Mechanochemical synthesis

학 번 : 2016-20297

# Table of Contents

# List of Table

## Chapter 2.



## Chapter 3.

# List of Figures

## Chapter 1.



## Chapter 2.

## Chapter 3.

irradiation under dose of $4 \times 10^{13}$ proton/cm$^2$. Adapted from Shin *et al.*

**Figure 3.15** Energy loss profiles of protons simulated via SRIM (a) in the full range and (b) in the range of 0–200 μm. (c) Schematics depicting the effects of proton beam irradiation on perovskite. Left image shows schematic for pristine perovskite, two images in the middle show schematics for perovskite irradiated under a low dose (left middle), in which the effect of hydrogen vacancies is dominant, and a high dose (right middle), in which the effects of lead and iodide vacancies increase. Right image shows schematic of self-healed perovskite in which hydrogen atoms released from bonds reassume their proper lattice positions. Adapted from Shin *et al.*

# Chapter 1. Introduction

## 1.1. Proton matter interaction

### 1.1.1 Energy loss process of irradiated charged particle

When charged particle such as a proton is irradiated to a target material, the proton loses energy by interacting with the material, and the process can be divided into two steps. First step is the electronic stopping process, which initially dominates until the protons are slowed down sufficiently. The other step is the nuclear stopping process, which dominates near the stopping depth, where the protons have been sufficiently decelerated. Electronic stopping process is an ionizing process in which incident protons create electron-hole pairs in the target material. In this process, protons lose energy homogeneously, causing the degradation on the target material such as a change in the threshold voltage. On the other hand, the nuclear stopping process includes all non-ionizing processes that damages the lattice structure of the target material. In this process, protons lose their energy rapidly and causes degradation of materials such as cracks in the oxide layer. Since the energy loss mechanism of irradiated particles is affected by the thickness of the target material, the stopping depth of the protons is one of the important factors in proton effect studies. The stopping depth is determined by the **stopping power** that is affected by factors such as the type of target material and the energy of the proton. We will discuss this in the next part.

### 1.1.2 Stopping power

Stopping power, which is the loss energy per unit path length of irradiated charged particles in a target material, can be expressed as a formula and the best known is the Bethe equation.

$$S(T) = -\frac{dT}{dx} = n_{ion}\bar{I} = \frac{4\pi z^2 e^2 nZ}{m\beta^2 c^2}\left[\ln\left(\frac{2mc^2\gamma^2\beta^2}{\bar{I}}\right) - \beta^2\right]$$

Here, T is the kinetic energy of the irradiated charged particle, $n_{ion}$ is the number of ionized atoms in target material, $\bar{I}$ is the average ionization energy, m is the mass of particle in the material that interact with irradiated particle, z is the charge number of incident particle (1 for proton), Z is the atomic number of target material, $\gamma$ is the lorentz factor and $\beta$ is the speed of the irradiated particle relative to the speed of light. Stopping power can be determined theoretically and experimentally with an accuracy of several % in the energy range of $0.1 \leq \beta\gamma \leq 1000$.

As can be seen from the Bethe equation, the stopping power increases as the speed of the proton decrease. While the irradiated particle travels through the material, its speed decreases and the stopping power increases toward the end of range. Shortly before the stopping depth where energy drops to zero, the force increases rapidly and reaches a maximum called as the Bragg peak. This tendency is also consistent with the simulation results in figure 1.1.

We simulated energy-loss profiles using Stopping and Range of Ions in Matter (SRIM) software. Figure 1.1 shows the SRIM results under various

irradiated proton energy of 1 MeV, 10 MeV, 100 MeV and 1 GeV. While the energy

of proton (which is related to the speed of the proton) increases by 10 to the third power from 1 MeV to 1 GeV, the stopping depth increases by 10 to the fifth power from 14.6 μm to 1.65 m. Also, the maximum value of energy lose per angstrom decreased from 12 to 0.18 eV/Å, as the proton energy increased. This show the stopping power decreases as the irradiated proton velocity increases.

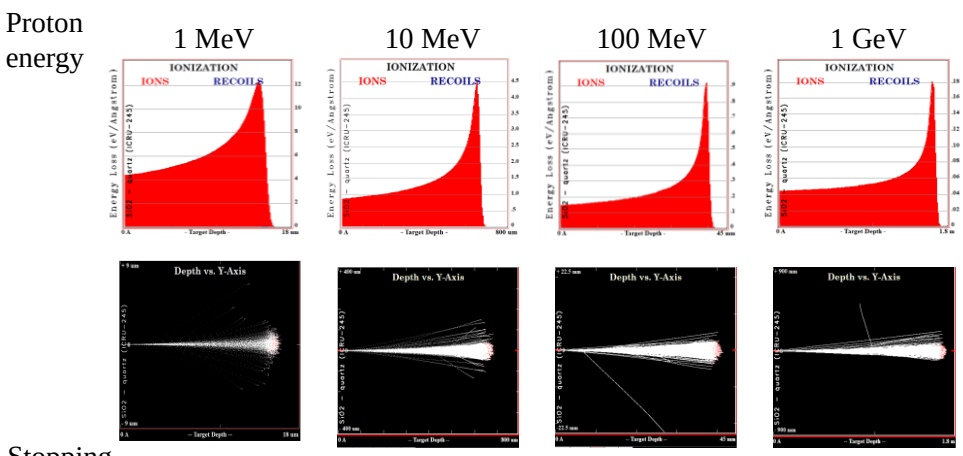


**Figure 1.1** SRIM results of various energy of proton beams

Other important factor influencing the stopping power is the type of target material. As the Beth equation shows, the stopping power is proportional to the atomic number. Figure 1.2 shows the SRIM results for various target materials

from beryllium (with atomic numbers 4) to lead (with atomic number 82) with proton energy of 10 MeV. As the atomic number increased from 4 to 82, the stopping depth decreased from 804 μm to 301 μm. This shows that the stopping power increases as the atomic number increases. Proton irradiation effect studies are being actively conducted by controlling these factors such as proton energy, and type and depth of target material according to the purpose of the study.

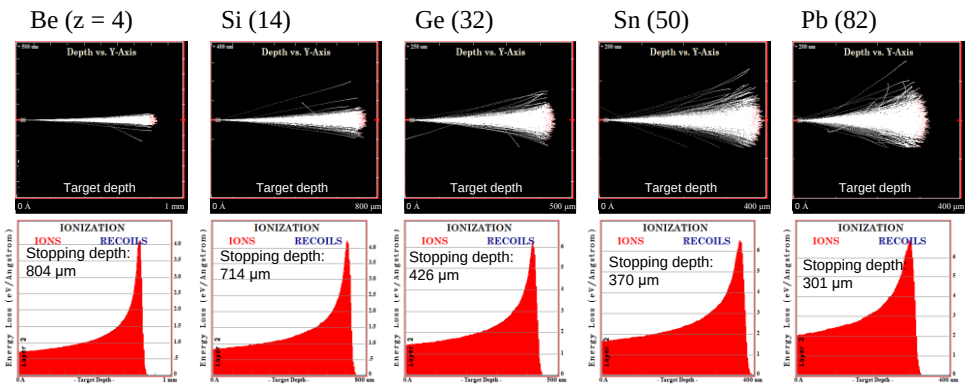


**Figure 1.2** SRIM results of various materials with atomic number from 4 to 82

## 1.2. Transition metal dichalcogenide and tungsten diselenide

Two-dimensional (2D) van der Waals materials which have strong in-plane covalent bonds and weak interlayer interactions such as graphene and transition-metal dichalcogenides (TMDCs) have been studied extensively because of their novel features. Two-dimensional materials can obtain atomically thin thickness film structures without dangling bonds, and this two-dimensional nature

realizes advantages such as high integration, high transparency and high flexibility. Also, the quantum confinement effect and reduced screening effect arising from this two-dimensional nature often manifest themselves in features clearly different from those of their bulk counterparts. Unlike graphene, which has no electric bandgap, TMDCs have various properties such as semi-metallic, semiconducting or superconducting properties depending on the combination of transition metal and chalcogens.

Among TMDC materials, $WSe_2$ has received considerable attention due to its unique electronic and optoelectronic properties, such as the existence of energy band gaps in the visible and near-infrared spectral ranges, and weak or non-existent Fermi level pinning at metal-$WSe_2$ interfaces. $WSe_2$ is a semiconducting material with a tuneable bandgap depending on thickness; 1.64 eV direct bandgap in monolayer and 1.2 eV indirect bandgap in bulk. In addition, the electric carrier type of $WSe_2$ is controllable through thickness; p-type with thin, ambipolar with intermediated, and n-type with thick thickness.

## 1.3. Organic-inorganic hybrid halide perovskite

### 1.3.1 Brief introduction of organic-inorganic hybrid halide perovskite and methylammonium lead iodide perovskite

A hybrid organic-inorganic halide perovskites (OIHPs) has a perovskite structure denoted with the structural formula $ABX_3$, where A is an organic cation, B is an inorganic cation and X is a halide. OIHP has received tremendous attention

in recent years due to its superior properties that depend on the combination of components for optoelectronics and electronic devices. Also, OIHPs have potential in space energy application owing to their attractive properties, such as high power-conversion efficiency, ultra-light weight, and large absorption coefficient.

### 1.3.2 Synthesis of $MAPbI_3$ perovskite

There are various ways to synthesize OIHP such as spin-coating methods, thermal evaporation methods, and mechanochemical synthesis. Out of various methods, Spin-coating methods are widely used in lab-scale fabrication because it is an easily accessible methods in terms of cost and time. However, spin-coating techniques have some challenges to be addressed such as solvent induced-damages, toxicity to human body, and producing reliable and uniform films over a large area.

On the other hand, dry synthesis methods such as thermal evaporation methods, and mechanochemical synthesis have the advantage that they do not require the use of solvents, allowing materials to be synthesized without solvent-induced damage, which is related to the performance of perovskite-based devices. In addition, the dry synthesis method has several additional advantages. Evaporation methods can produce a uniform film over a large area on the wafer scale. In the case of mechanochemical synthesis, not only stoichiometric fine control is possible with very small amount of by-product, so perovskite with small defects can be synthesized. but also easy to accessible and rapid synthesis. Also, the dry synthesis method can produce OIHP films with a wide range of compositions by combining various cations and halides.

## 1.4. Outline of this thesis

This thesis mainly focuses on the high energy proton irradiation effect on promising nanomaterials such as $WSe_2$ of transition metal dichalcogenides and $MAPbI_3$ of OIHP with various dose conditions. The major reason for exploring effects of proton irradiation on nanomaterials during my doctorate course is to broaden our understanding of the interaction between irradiated protons and target materials and examine the potential of device applications in a high-radiation environment such as space.

In Chapter 2, the study of the changes in the electrical characteristics of $WSe_2$ field effect transistor after the various dose of proton irradiation are discussed. These changes can be explained by proton irradiation-induced traps such as “positive bulk trap” in oxide layer and “negative interface trap state” at the interface between the oxide layer and $WSe_2$. In Chapter 3, I discuss the high energy proton radiation hardness of methylammonium lead iodide perovskite synthesized by two kind of methods; flash-evaporation and mechanochemical synthesis. The radiation hardness of proton beam varies depending on the synthesis method of perovskite because the bonding strength in the synthesized perovskite vary depending on the synthesis method. Finally, Chapter 4 summaries this thesis and suggests directions for future research.

# Chapter 2. Effect of Proton Beam Irradiation on $WSe_2$ Ambipolar FETs

## In this chapter…

*The irradiation effect of high energy proton beams on tungsten diselenide ($WSe_2$) ambipolar field-effect transistors was investigated. We measured the electrical characteristics of the fabricated $WSe_2$ FETs before and after the 10 MeV proton beam irradiation with different doses of $10^{12}$, $10^{13}$, $10^{14}$, and $10^{15}$ $cm^{-2}$. For low dose conditions ($10^{12}$, $10^{13}$, and $10^{14}$ $cm^{-2}$), the threshold voltages shifted to the negative gate voltage direction, and the current in the hole and electron accumulation regimes decreased and increased, respectively. However, the trends were opposite for the high dose condition ($10^{15}$ $cm^{-2}$); the threshold voltages shifted to the positive gate voltage direction, and the current in the hole and electron accumulation regimes increased and decreased, respectively. These phenomena can be explained by the combined effect of proton irradiation-induced traps and the applied gate bias condition. Specifically, irradiation-induced positive oxide traps in $SiO_2$ dielectric play a role in enhancing electron accumulation and reducing hole accumulation in the $WSe_2$ channel, whereas the irradiation-induced holes near the $WSe_2/SiO_2$ interface act as electron trapping sites, with enhancing*

*hole accumulation and reducing electron accumulation in the $WSe_2$ channel. This work will help improve the understanding of the effect of high energy irradiation on $WSe_2$-based and other ambipolar nanoelectronic devices. In addition, this work shows the possibility of tuning the electrical properties of $WSe_2$-based devices.*

## 2.1. Introduction

Two-dimensional (2D) semiconducting transition-metal dichalcogenides (TMDs) have gained significant attention due to their unique electronic and optoelectronic properties, the presence of energy band gaps from the visible and near infrared spectral range, and atomically thin film structures.[1-6] To date, tremendous efforts have been devoted to designing and synthesizing 2D TMDs and to exploring their potential applications.[2,7-14] Therefore, understanding the fundamental mechanisms and controlling the properties of 2D TMDs is crucial for further versatile applications in integrated devices including energy systems, light emitting devices, field effect transistors (FETs) and photodetectors.[3,5,6,10,15-19]

The material properties of 2D TMDs can be effectively tuned through various methods such as dimension reduction, heterostructure formation, intercalation, doping, strain engineering, and especially the irradiation effects of ions or electrons.[3,13,19-31] In particular, most irradiation studies to date have been focused on single type charge carriers in TMDs devices.[29-31] Among 2D TMDs, tungsten diselenide ($WSe_2$) has recently been studied from the perspective of irradiation effects of ion- and electron-beams.[32-35] $WSe_2$ has many excellent

properties, such as a tunable bandgap (1.2–1.67 eV), ambipolar transport behaviour, and weak or nonexistent Fermi level pinning at metal-$WSe_2$ interfaces;[3,25,36] these properties make 2D $WSe_2$ a promising candidate for potential device applications, including valley-based electronics, spin-electronics, and optoelectronics.[23,37-39] To the best of our knowledge, there is no report on the electrical transport properties of $WSe_2$ FETs showing p-type and n-type conduction through irradiation of high energy proton beams.

In this work, we studied the effect of high energy proton beam irradiation on the ambipolar $WSe_2$ FETs. The devices were irradiated with 10 MeV energy protons under different dose conditions of $10^{12}$, $10^{13}$, $10^{14}$ and $10^{15}$ $cm^{-2}$. The electrical characteristics of the $WSe_2$ FETs such as current level and threshold voltages were measured before and after the proton beam irradiation, and the changes after the irradiation were analysed statistically. Additionally, we measured physicochemical properties such as lattice vibration, binding energy, and thickness of the $WSe_2$ flakes using Raman spectra, AFM, and X-ray photoelectron spectra. After the proton beam irradiation, the electrical properties were changed due to the irradiation-induced traps from the substrate, not from the $WSe_2$ itself.

## 2.2. Experiments

### 2.2.1 Device fabrication process of $WSe_2$ FETs

Figure 2.1 illustrates the device fabrication processes for $WSe_2$ ambipolar FETs. First, a highly doped p-type Si wafer with 270 nm thick $SiO_2$ layer was

prepared. The $WSe_2$ flakes were transferred onto the silicon substrate by the mechanical exfoliation using a scotch tape from a bulk $WSe_2$ crystal (purchased from HQ Graphene). Using an optical microscope, candidate $WSe_2$ flakes with a few layers thickness range from 4 to 7 nm were selected to make ambipolar type $WSe_2$ FETs. (Table 2.1) The thicknesses of $WSe_2$ flakes were measured using an atomic force microscope (AFM) (Park Systems, NX10). Then, we spin-coated a bi-layer electron beam resist; first methyl methacrylate (MMA) (8.5) MAA (9% concentration in ethyl lactate) was spin-coated on the samples at 4,000 rpm for 50 s, and then the samples were baked on a hotplate at 180 °C for 90 s. Next, poly methyl methacryllate (PMMA) 950K (5% concentration in anisole) was spin-coated on MMA-coated samples at 4,000 rpm for 50 s, followed by a bake on the hotplate at 180 °C for 90 s. Then, we patterned the source and drain electrodes using an electron beam lithography (JEOL, JSM-6510) and performed development process with methyl isobutyl ketone: isopropyl alcohol (MIBK:IPA) (1:3) solution for 50 s. Finally, we deposited Au (40 nm)/Ti (5 nm) as the source and drain electrodes using an electron beam evaporator.

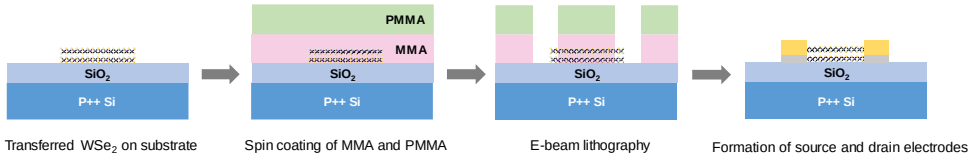


**Figure 2.1** Schematics of $WSe_2$ device fabrication. Adapted from Shin *et al.* [52]

### 2.2.2 Electrical and optical characteristics measurements

The electrical characteristics of the fabricated devices were measured in a probe station (ST-500, JANIS) using a semi-conductor parameter analyzer (Keithley 4200 SCS) in vacuum (~$10^{-4}$ Torr). Raman spectra of $WSe_2$ flakes were measured by using a Raman spectroscopy (XperRam 200, Nanobase, Inc.) with a 532 nm laser as the excitation source. The laser power was 40 μW with a diffraction-limited laser spot size of ~1 μm. The XPS spectra were measured by electron spectroscopy for chemical analysis (AXIS SUPRA) in National Center for Inter-university Research Facilities.

### 2.2.3 Proton beam irradiation experiment

The fabricated devices were exposed to proton beams with different dose conditions of $10^{12}$, $10^{13}$, $10^{14}$, and $10^{15}$ $cm^{-2}$. The proton beam facility used for this research was the MC-50 cyclotron at the Korea Institute of Radiological and Medical Sciences. The proton beam had an energy of 10 MeV with an average current 10 nA, corresponding to irradiated $6.25 \times 10^{10}$ protons per seconds. All the measurement for the proton-irradiated devices was taken one day after the proton irradiation since the radioactivity had to fall below the safe level.

## 2.3. Results and discussion

### 2.3.1 Electrical characteristics

The $WSe_2$ FETs were fabricated with mechanically exfoliated $WSe_2$ flakes on heavily p-doped Si substrates with a 270 nm-thick $SiO_2$ dielectric layer. Fig. 2.2 (a) is the optical image of a transferred $WSe_2$ flake on the Si/$SiO_2$ substrate. The $WSe_2$ flake shown in Fig. 2.2 (a) was found to be ~4 nm-thick using an atomic force microscope (AFM) (Fig. 2.2 (b)). Fig. 2.2 (c) shows the optical image of a $WSe_2$-based device made with the flake shown in Figs. 2.2 (a) and 2.2 (b).

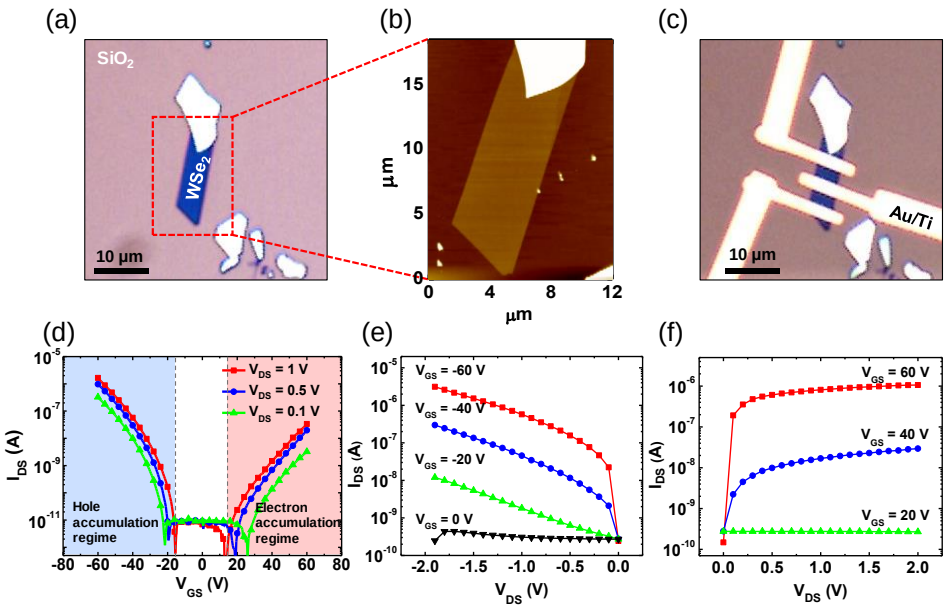


**Figure 2.2** (a) An optical image of a multilayer $WSe_2$ flake. (b) An AFM image of the selected region in (a) with cross-sectional profile across a line in the image. (c) An optical image of the fabricated FET using this $WSe_2$ flake. (d) The transfer curves of the fabricated $WSe_2$ FET measured at $V_{DS}$ = 0.1 V, 0.5 V, and 1 V. The output curves for (e) negative gate voltages and (f) positive gate voltages measured at different gate voltages. Adapted from Shin *et al.* [52]

The electrical properties of the fabricated $WSe_2$ FET were examined, as shown in Figs. 2.2 (d)-2.2 (f). Transfer characteristics (drain-source current versus gate voltage, $I_{DS}$–$V_{GS}$) (Fig. 2.2 (d)) and output characteristics (drain-source current versus drain-source voltage, $I_{DS}$–$V_{DS}$) (Figs. 2.2 (e) and 2.2 (f)) show a sharp increase of $I_{DS}$ at both negative (the hole accumulation regime, marked by blue colour) and positive (the electron accumulation regime, marked by red colour) gate voltages, indicating the gate-induced charge injection from metal/$WSe_2$ contacts. According to Podzorov *et al.*[40], the Schottky-type FETs exhibit ambipolar characteristics by gate-controlled tunneling of injected charges (hole and electron) through the Schottky barriers formed at the metal/$WSe_2$ semiconductor contacts. The electrical properties of other ambipolar $WSe_2$ FETs show in the Fig. 2.3 and Table 2.1.

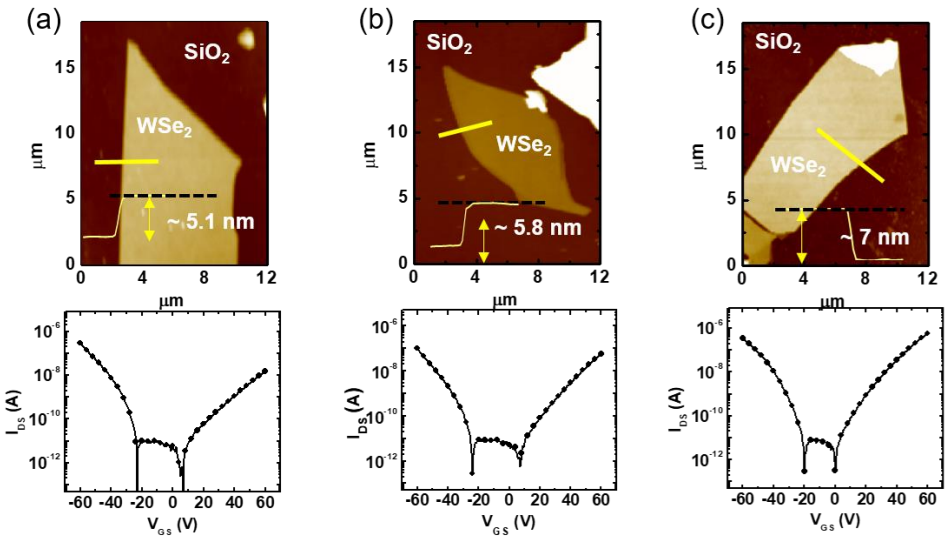


**Figure 2.3** The AFM images of $WSe_2$ flakes and corresponding transfer curves of the $WSe_2$ FETs with thickness of (a) 5.1 nm, (b) 5.8 nm, and (c) 7 nm. Adapted from Shin *et al.* [52]

**Table 2.1** The previous studies of thickness-dependent electrical conduction type of $WSe_2$ FETs

| Thickness (nm) | | | Electrode | Reference |
|---|---|---|---|---|
| p-type | ambipolar | n-type | | |
| <4 | ~6 | >15 | Ni/Au | [23] |
| | 7–26 | | Ti/Au | [32] |
| | 6 | | S: Ni, D: Pd | [36] |
| <3 | ~4 | >5 | Cr/Au | [53] |
| | 4-7 | | Ti/Au | [52] |

### 2.3.2 Proton beam dose-dependence

After electrical characterization of the fabricated $WSe_2$ FETs, the devices were subsequently irradiated by proton beams of 10 MeV for 10, 100, 1000, and 10000 seconds, corresponding to dose values of ~$10^{12}$, $10^{13}$, $10^{14}$, and $10^{15}$ $cm^{-2}$, respectively. The electrical characteristics of $WSe_2$ FETs were measured and compared before and after proton beam irradiation, as shown in Fig. 2.4 and Fig. 2.5.

In the transfer curves of the device measured at fixed $V_{DS}$ = 1 V, both the threshold voltages for hole and electron accumulation regimes shifted to the negative gate voltage direction after the proton beam irradiation for the dose of ~$10^{12}$, $10^{13}$, and $10^{14}$ $cm^{-2}$ (Figs. 2.4 (a)-2.4 (c)). The drain-source current level of the hole accumulation regime decreased, whereas that of the electron accumulation regime increased. For example, after the proton beam irradiation under a $10^{12}$ $cm^{-2}$ dose, the drain-source current decreased from 0.11 μA to 0.04 μA at $V_{DS}$ = 1 V and $V_{GS}$ = –60 V for the hole accumulation regime, and it increased from 0.06 μA to 0.31 μA at $V_{DS}$ = 1 V and $V_{GS}$ = 60 V for the electron accumulation regime (Fig. 2.4 (a)). In the low irradiation dose conditions of ~$10^{12}$, $10^{13}$, and $10^{14}$ $cm^{-2}$, the shifted amount of the threshold voltage seemed to increase as the dose increased (marked by blue and red arrows in Figs. 2.4 (a)-2.4 (c)).

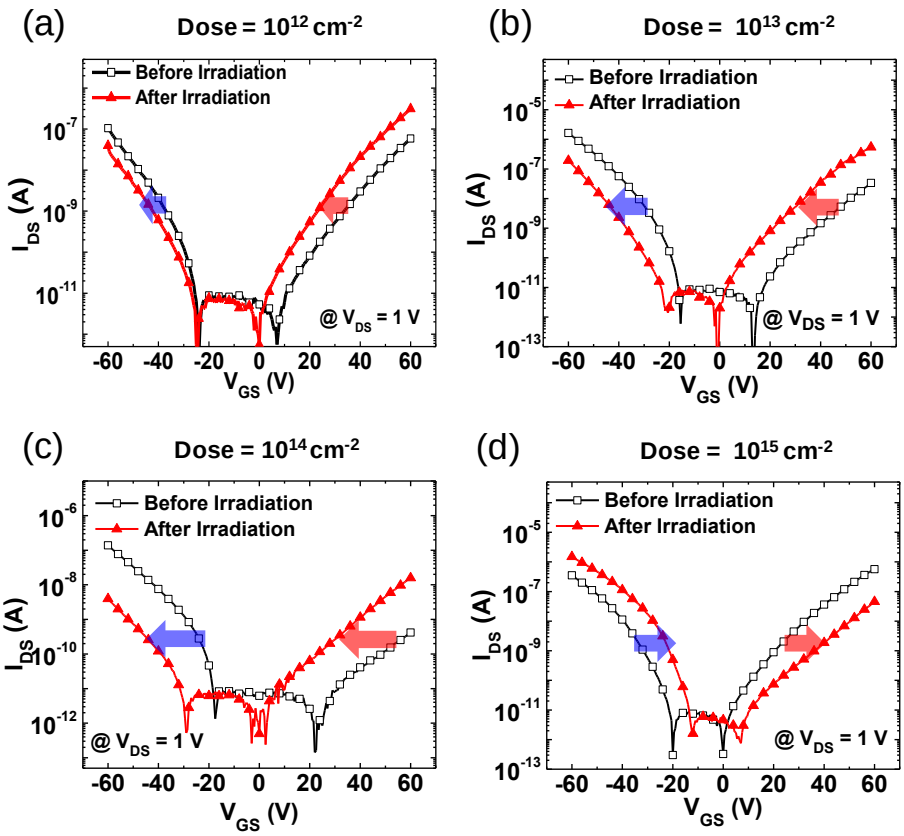


**Figure 2.4** Transfer curves of the WSe2 FETs before and after proton beam irradiation under the doses of (a) $10^{12}$, (b) $10^{13}$, (c) $10^{14}$, and (d) $10^{15}$ $cm^{-2}$. Adapted from Shin et al. [52]

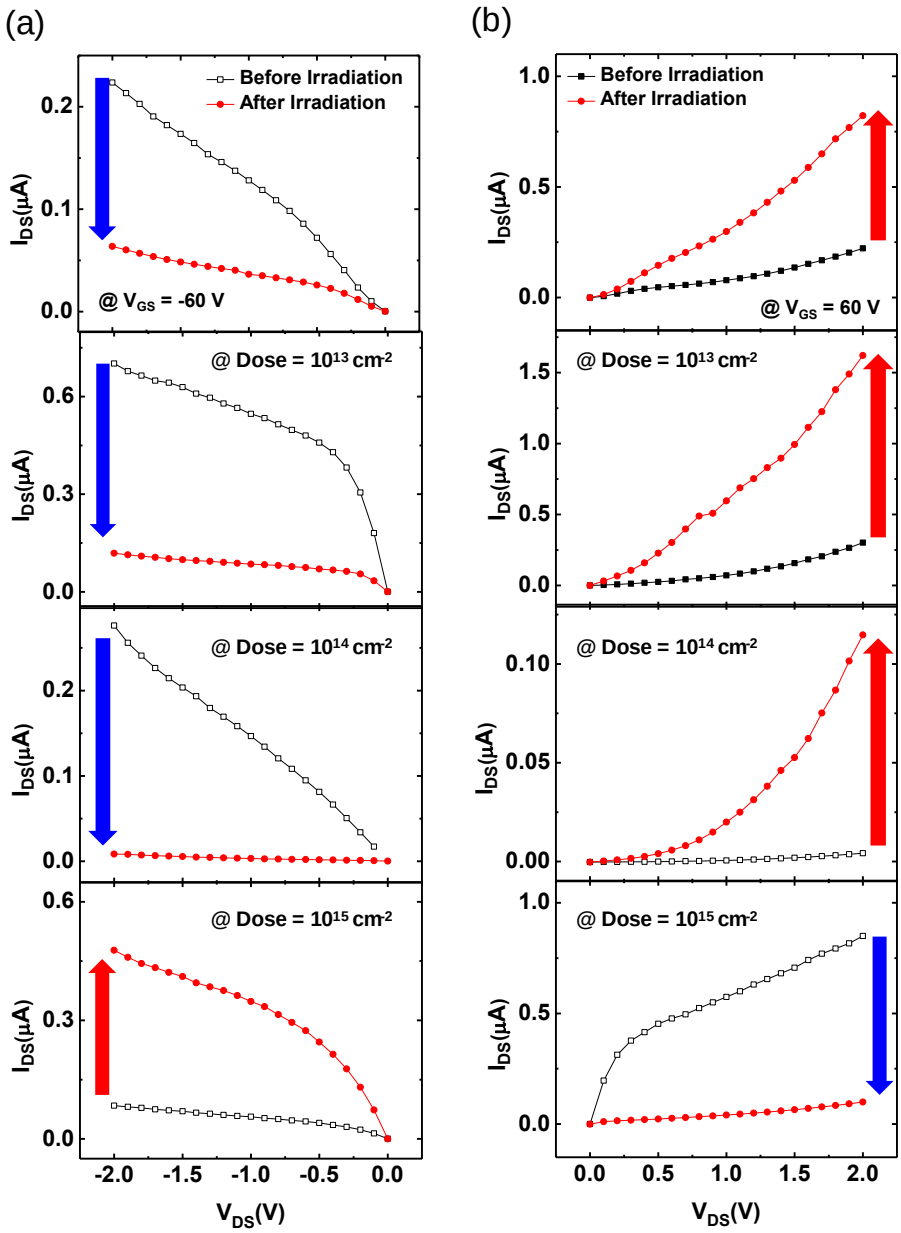


**Figure 2.5** The output characteristics with proton beam irradiation dose conditions of $10^{12}$, $10^{13}$, $10^{14}$, and $10^{15}$ $cm^{-2}$ for (a) hole and (b) electron accumulation regimes. Adapted from Shin *et al.* [52]

Correspondingly, the amount of current change in the hole and electron accumulation regimes became larger as the dose increased (Figs. 2.4 (a)-2.4 (c)). For example, after the proton beam irradiation under a $10^{14}$ $cm^{-2}$ dose, the drain-source current decreased from 140 nA to 4 nA at $V_{DS}$ = 1 V and $V_{GS}$ = –60 V for the hole accumulation regime, and it increased from 0.4 nA to 16 nA at $V_{DS}$ = 1 V and $V_{GS}$ = 60 V for the electron accumulation regime (Fig. 2.4 (c)). However, the $WSe_2$ FETs that were irradiated with a proton beam dose of $10^{15}$ $cm^{-2}$ showed different behaviour compared to the devices irradiated under low dose conditions (Fig. 2.4 (d)). After proton beam irradiation under a $10^{15}$ $cm^{-2}$ dose, the threshold voltages shifted to the positive gate voltage direction for both hole and electron accumulation regimes, and the drain-source current increased in the hole accumulation regime while it decreased in the electron accumulation regime. These dose-dependent phenomena of proton beam irradiation will be explained in detail later in terms of the combined effects by irradiation-induced charges and gate-bias condition.

### 2.3.3 Statistical analysis of electrical properties

To clarify these different trends between the two cases of low and high proton beam doses, we statistically investigated the changes of current and threshold voltage as a function of proton beam dose. We measured a total of 20 devices, with 4–6 devices for each proton beam irradiation condition. Figs. 2.6 (a)

and 2.6 (b) summarize the changes of threshold voltages for the $WSe_2$ FETs after the proton beam irradiation under dose conditions of $10^{12}$, $10^{13}$, $10^{14}$, and $10^{15}$ $cm^{-2}$

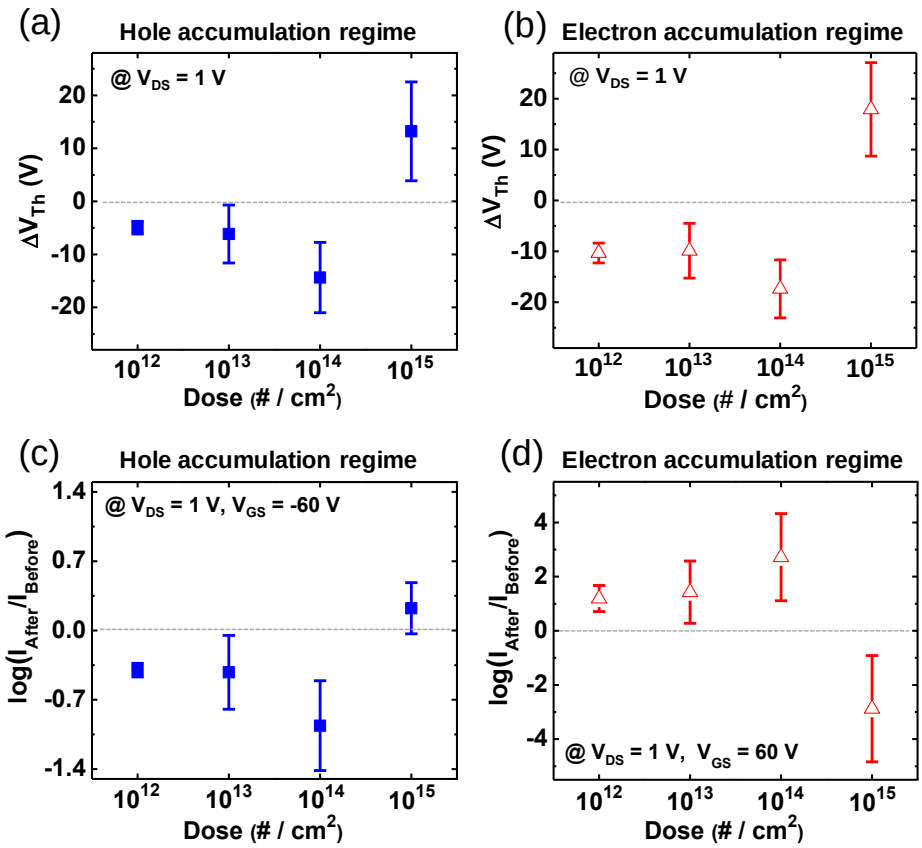


**Figure 2.6** Threshold voltage shift measured at $V_{DS}$ = 1 V as a function of proton irradiation dose condition for (a) hole accumulation regime and (b) electron accumulation regime. The normalized $I_{DS}$ (current ratio before and after irradiation, $I_{after}/I_{before}$) measured at $V_{DS}$ = 1 V as a function of proton irradiation dose condition for (c) hole accumulation regime and (d) electron accumulation regime. Adapted from Shin *et al.* [52]

for hole and electron accumulation regimes at $V_{DS}$ = 1 V, respectively. Note that the threshold voltage was determined by the value of x-intercept of the tangent line from the point that has the maximum differential value in the transfer curve. In Figs. 2.6 (a) and 2.5 (b), similar to Fig. 2.4, the threshold voltages for both hole and electron accumulation regimes moved to negative gate voltage direction for low dose conditions of ~$10^{12}$, $10^{13}$, and $10^{14}$ $cm^{-2}$. In addition, as the irradiation dose increased, the threshold voltages shifted more. However, the threshold voltage of the devices irradiated with high dose proton beam ($10^{15}$ $cm^{-2}$) shifted to the positive gate voltage direction. Figs. 2.6 (c) and 2.6 (d) summarize the changes of the device current after the proton beam irradiation for hole and electron accumulation regimes, respectively.

The currents in these Figs. are the values measured at $V_{DS}$ = 1 V with $V_{GS}$ = −60 V for the hole accumulation regime and $V_{GS}$ = 60 V for the electron accumulation regime. The device current for the hole accumulation regime (Fig. 2.6 (c)) decreased as the irradiation dose increased to $10^{14}$ $cm^{-2}$, and then it increased at the dose of $10^{15}$ $cm^{-2}$. The current showed an opposite tendency for the electron accumulation regime (Fig. 2.6 (d)); the current increased as the irradiation dose increased to $10^{14}$ $cm^{-2}$, and then it decreased at the dose of $10^{15}$ $cm^{-2}$. As we mentioned above, these results can be explained by the irradiation-induced positive oxide traps in the gate dielectric $SiO_2$ layer and electron trapping at the interface between $SiO_2$ and $WSe_2$. Note that mobility and subthreshold swing values are also summarized as a function of proton dose in Figs. 2.7 and 2.8. The mobility of the ambipolar $WSe_2$ FET devices was calculated using the following equation:

$$\mu = \frac{L}{W}\frac{1}{C_i V_{DS}}\frac{dI_{DS}}{dV_{GS}}$$

where $L$ and $W$ are the channel length and width of the FET, respectively. $V_{DS}$ is the source−drain voltage. $I_{DS}$ is the current flowing from source to drain, and $V_{GS}$ is the gate voltage. $C_i$ is the gate capacitance per unit area. But mobility and subthreshold swing values did not show a clear trend with the dose conditions as the threshold voltages or currents did.

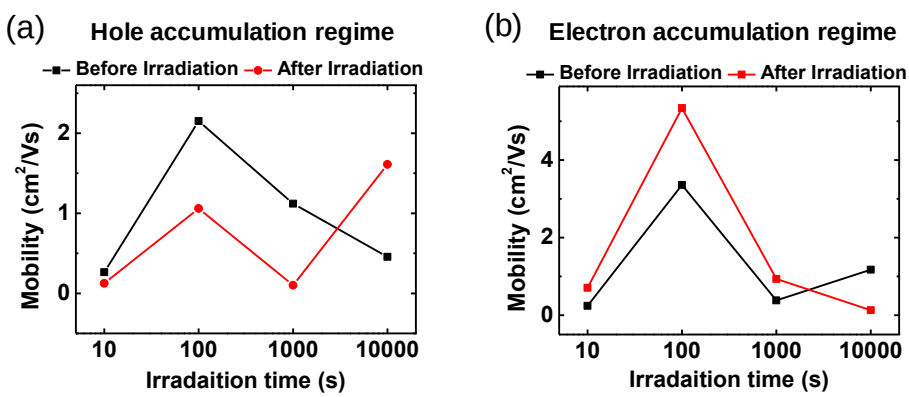


**Figure 2.7** Mobility of the devices before and after the proton beam irradiation for (a) hole and (b) electron accumulation regimes. Adapted from Shin *et al.* [52]

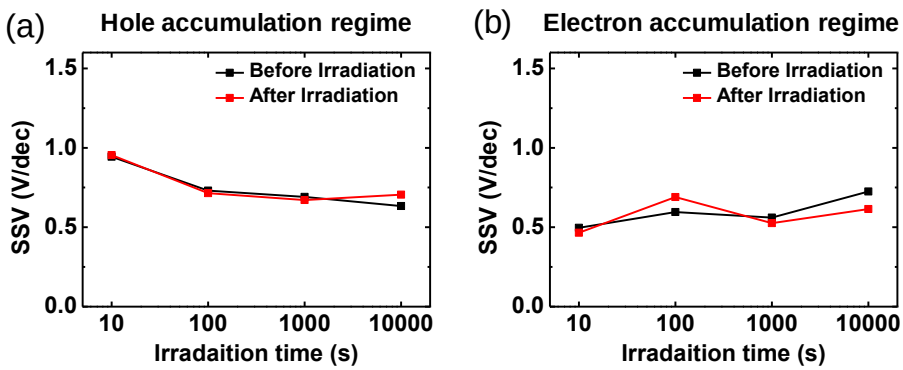


**Figure 2.8** Subthreshold swing value of the devices before and after the proton beam irradiation for (a) hole and (b) electron accumulation regimes. Adapted from Shin *et al.* [52]

### 2.3.4 Physicochemical properties of $WSe_2$ flakes

To verify whether such variations of electrical characteristics are caused by proton beam-irradiated $WSe_2$ flakes themselves, we examined the structural characteristics, elemental composition, and electronic state of $WSe_2$ flakes before and after the proton beam irradiation by Raman spectroscopy and X-ray photoemission spectroscopy (XPS). Fig. 2.9 shows the measured results for the high dose condition of $10^{15}$ $cm^{-2}$. Raman mapping data of the $WSe_2$ flake (Figs. 2.9 (a) and 2.9 (b)) show no noticeable differences before and after proton beam irradiation. Specifically, in Raman spectra (Fig. 2.9 (c)), the position and intensity of three prominent Raman peaks corresponding to lattice vibration mode of $E^1_{2g}$ (254 $cm^{-1}$), $A_{1g}$ (254 $cm^{-1}$ and 264 $cm^{-1}$), and $B^1_{2g}$ (310 $cm^{-1}$)[38,41,42] were not noticeably changed after proton beam irradiation. The XPS result (Fig. 2.9 (d))

shows three dominant binding energy peaks of tungsten and two dominant peaks of selenium.[42,43] These five peaks did not show considerable change after proton beam irradiation. Note that a little redshift (by ~0.1 eV) was observed after proton beam irradiation (Fig. 2.9 (d)), which may have originated from a dipole effect due to the irradiation-induced electron trapping at the interface between $SiO_2$ and $WSe_2$ with van der Waals gap.[44-46] As a result, the physicochemical characteristics of $WSe_2$ were not damaged by proton beam irradiation, and therefore, the change of the electrical characteristics after proton beam irradiation is not considered to be caused by the $WSe_2$ itself.

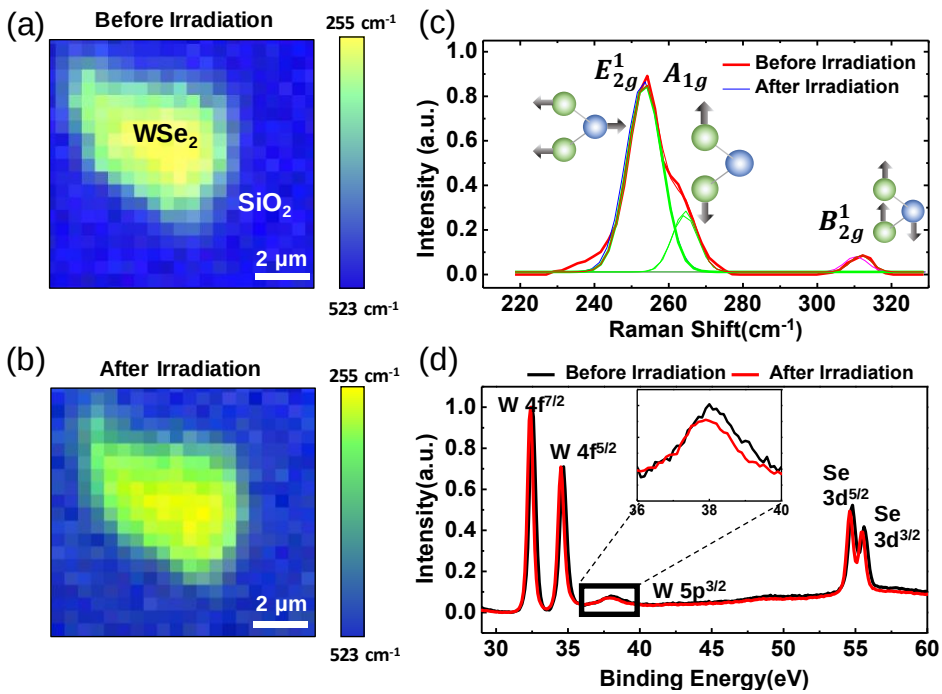


**Figure 2.9** (a, b) Raman mapping, (c) Raman spectra, and (d) XPS spectra of $WSe_2$ flakes before and after proton irradiation at a dose of $10^{15}$ $cm^{-2}$. Adapted from Shin *et al.* [52]

### 2.3.5 Mechanism of proton irradiation effect

The experimental results can be explained by the combined effects of the proton beam irradiation-induced traps and applied gate bias condition. When high-energy protons are irradiated on the $WSe_2$ FETs, protons generate various kinds of traps. The high energy protons slow down mainly by an electronic stopping process, generating electron-hole pairs. After the protons sufficiently slow down, they lose the majority of the energy by a nuclear stopping process, and then they stop near the stopping depth and damage on the lattice around the stopping depth.[47-49] To calculate the stopping depth, we simulated energy-loss profiles using Stopping and Range of Ions in Matter (SRIM) software. According to the SRIM results, most of the protons with 10 nA current and 10 MeV energy would stop near 700 μm from the surface (Fig. 2.10). Since the thickness of the device is approximately 500 μm (4–7 nm for the $WSe_2$ flake, 270 nm for the $SiO_2$ layer, and 500 μm for the Si layer), most of the protons would penetrate through the entire device structure and electron-hole pairs are generated along the paths.

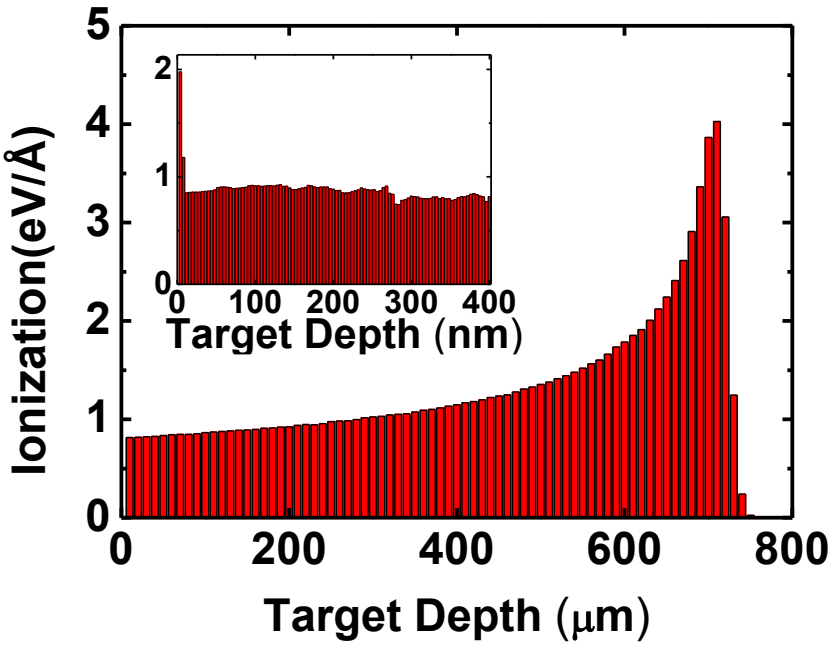


**Figure 2.10** The energy loss profiles of the protons simulated by SRIM. The inset image is a zoomed result for the range of 0-400 nm from the top surface which includes the oxide layer. Adapted from Shin *et al.* [52]

The $SiO_2$ layer is the most sensitive to the ionizing process. After electron-hole pairs are generated, they recombine for a few picoseconds, but some of the holes remained near the generated location while electrons are swept away much faster.[50,51] The trapped holes in the $SiO_2$ layer (denoted as "positive oxide traps") cause the modulation of gate electric field, resulting in the depletion effect of holes and enhancement effect of electrons in the $WSe_2$ channel (Figs. 2.11 (a) and 2.11 (c)). Some of the generated holes undergo an anomalous stochastic hopping transport through the $SiO_2$ layer and reach the $WSe_2/SiO_2$ interface under the high

dose condition (Figs. 2.11 (e) and 2.11 (g)). These holes that reach the interface can cause the formation of a layer of electron trapping sites, resulting in the enhancement effect of holes and depletion effect of electrons in the $WSe_2$ channel (Figs. 2.11 (e) and 2.11 (g)). As a result, positive oxide traps play a role in enhancing electron accumulation and reducing hole accumulation in the $WSe_2$ channel, whereas the electron trapping sites near the $WSe_2/SiO_2$ interface (denoted as "interface electron trap sites") enhance hole accumulation in the $WSe_2$ channel. Because the interface electron trap sites require a longer proton irradiation time than the positive oxide traps, the effect of the positive oxide traps in $SiO_2$ bulk is more influential for low dose conditions ($10^{12}$, $10^{13}$, and $10^{14}$ $cm^{-2}$) (Figs. 2.11 (a)–2.11 (d)). In the energy band diagrams, due to the positive oxide traps, electrons are efficiently injected into the $WSe_2$ channel under positively applied gate voltage (Fig. 2.11 (b)) while it becomes difficult to inject holes into the $WSe_2$ channel under negatively applied gate voltage (Fig. 2.11 (d)). Thus, the threshold voltage shifts to the negative gate voltage direction (Figs. 2.4 (a)-2.4 (c), 2.6 (a) and 2.6 (b)). As the proton beam irradiation dose increases, more positive oxide traps are generated. Therefore, the threshold voltage shift can be larger because the positive oxide traps increase as the proton beam irradiation dose increases, as shown in Figs. 2.6 (a)-2.6 (b). However, in the high dose condition of $10^{15}$ $cm^{-2}$, the effect of interface electron trap sites becomes dominant, and therefore, the threshold voltage shifts to the positive gate voltage direction (Figs. 2.4 (d), 2.6 (a) and 2.6 (b)). Here, it becomes difficult to inject electrons into the $WSe_2$ channel (Fig. 2.11 (f)) and easier to inject holes into the $WSe_2$ channel (Fig. 2.11 (h)).

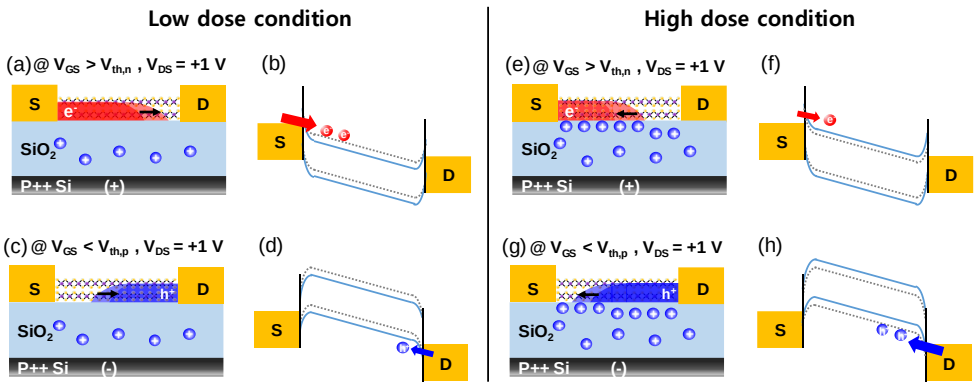


**Figure 2.11** Schematic illustrations of device structure and energy band diagrams depicting the conduction mechanism after proton beam irradiation. For low dose conditions ($10^{12}$, $10^{13}$, and $10^{14}$ $cm^{-2}$), the effect of positive oxide traps is dominant, resulting in the enhancement of electron accumulation in the channel (a, b, c, d). For the high dose condition ($10^{15}$ $cm^{-2}$), the effect of interface electron trap sites is dominant, resulting in the enhancement of hole accumulation in the channel (e, f, g, h). Adapted from Shin *et al.* [52]

## 2.4 Conclusions

In summary, we investigated the irradiation effect of a high-energy (10 MeV) proton beam on the $WSe_2$ FETs with ambipolar characteristics. The electrical properties such as the current and threshold voltages of the $WSe_2$ devices were changed after proton beam irradiation, depending on the beam dose conditions due to the combing effect of the proton beam irradiation-

induced charges and applied gate bias. Under low dose conditions ($10^{12}$, $10^{13}$, and $10^{14}$ $cm^{-2}$), the positive trapped holes in the $SiO_2$ dielectric layer produces the modulation of effective gate field on electron and hole accumulation to the $WSe_2$ channel, resulting in a threshold voltage shift towards the negative gate voltage direction. Under the high dose condition ($10^{15}$ $cm^{-2}$), the irradiation-induced holes near the $WSe_2/SiO_2$ interface act as electron-trapped sites and enhance hole accumulation in the $WSe_2$ channel, resulting in a threshold voltage shift towards the positive gate voltage direction. This study may provide a method to control the electrical properties of $WSe_2$ FETs through proton beam irradiation. Furthermore, this study may contribute to a deeper understanding of the influence of high-energy proton beams on ambipolar $WSe_2$-based nanoelectronic devices and be helpful for application of TMD-based devices in harsh radiation environments such as space.

## References

1. K. F. Mak, C. Lee, J. Hone, J. Shan and T. F. Heinz, Atomically Thin $MoS_2$: A New Direct-Gap Semiconductor. *Phys. Rev. Lett.*, 2010, **105**, 136805.
2. Q. H. Wang, K. Kalantar-Zadeh, A. Kis, J. N. Coleman and M. S. Strano, Electronics and Optoelectronics of Two-Dimensional Transition Metal Dichalcogenides. *Nat. Mater*., 2012, **7**, 699-712.
3. H. Wang, H. Yuan, S. S. Hong, Y. Li and Y. Cui, Physical and Chemical Tuning of Two-Dimensional Transition Metal Dichalcogenides. *Chem. Soc. Rev.* 2015, **44**, 2664-2680.
4. B. Radisavljevic, A. Radenovic, J. Brivio, V. Giacometti and A. Kis, Single-Layer $MoS_2$ Transistors. *Nat. Nanotechnol.*, 2011, **6**, 147-150.
5. K. F. Mak and J. Shan, Photonics and Optoelectronics of 2D Semiconductor Transition Metal Dichalcogenides. *Nat. Photonics*, 2016, **10**, 216-226.
6. J. Y. Lee, J.-H. Shin, G.-H. Lee, and C. H. Lee, Two-Dimensional Semiconductor Optoelectronics Based on van der Waals Heterostructures. *Nanomaterials*, 2016, **6**, 193.
7. T. Mueller and E. Malic, Exciton Physics and Device Application of Two-Dimensional Transition Metal Dichalcogenide Semiconductors. *NPJ 2D Mater. Appl.*, 2018, **2**, 29.
8. R. Lv, J. A. Robinson, R. E. Schaak, D. Sun, Y. Sun, T. E. Mallouk and M. J. Terrones, Transition Metal Dichalcogenides and Beyond: Synthesis, Properties, and Applications of Single-and Few-Layer Nanosheets. *Acc. Chem. Res*., 2014, **48**, 56-64.

9. N. Choudhary, M. R. Islam, N. Kang, L. Tetard, Y. Jung, and S. I. Khondaker, Two-Dimensional Lateral Heterojunction through Bandgap Engineering of $MoS_2$ via Oxygen Plasma. *J. Phys. Condens. Matter*, 2016, **28**, 364002.
10. W. Huh, S. Jang, J. Y. Lee, D. Lee, D. Lee, J. M. Lee, H. -G. Park, J. C. Kim, H. Y. Jeong, G. Wang, and C.-H. Lee, Synaptic Barristor Based on Phase-Engineered 2D Heterostructures. *Adv. Mater.*, 2018, **30**, 1801447.
11. X. Liu, I. Balla, H. Bergeron, G. P. Campbell, M. J. Bedzyk and M. C. Hersam, Rotationally Commensurate Growth of $MoS_2$ on Epitaxial Graphene. *ACS Nano*, 2016, **10**, 1067-1075.
12. I. S. Kim, V. K. Sangwan, D. Jariwala, J. D. Wood, S. Park, K.-S. Chen, F. Shi, F. Ruiz-Zepeda, A. Ponce, M. Jose-Yacaman, V. P. Dravid, T. J. Marks, M. C. Hersam and L. J. Lauhon, Influence of Stoichiometry on the Optical and Electrical Properties of Chemical Vapor Deposition Derived $MoS_2$. *ACS Nano*, 2014, **8**, 10551-10558.
13. D. Jariwala, S. L. Howell, K.-S. Chen, J. Kang, V. K. Sangwan, S. A. Filippone, R. Turrisi, T. J. Marks, L. J. Lauhon and M. C. Hersam, Hybrid, Gate-Tunable, van der Waals p–n Heterojunctions from Pentacene and $MoS_2$. *Nano Lett.*, 2016, **16**, 497-503.
14. H. Bergeron, V. K. Sangwan, J. J. McMorrow, G. P. Campbell, I. Balla, X. Liu, M. J. Bedzyk, T. J. Marks and M. C. Hersam, Chemical Vapor Deposition of Monolayer $MoS_2$ Directly on Ultrathin $Al_2O_3$ for Low-Power Electronics. *Appl. Phys. Lett.*, 2017, **110**, 053101.

15. W. Choi, N. Choudhary, G. H. Han, J. Park, D. Akinwande and Y. H. Lee, Recent Development of Two-Dimensional Transition Metal Dichalcogenides and Their Applications. *Mater. Today*, 2017, **20**, 116-130.
16. A. Pospischil, M. M. Furchi and T. Mueller, Solar-Energy Conversion and Light Emission in an Atomic Monolayer p–n Diode. *Nat. Nanotechnol.*, 2014, **9,** 257-261.
17. S. S. Varghese, S. H. Varghese, S. Swaminathan, K. K. Singh and V. Mittal, Two-Dimensional Materials for Sensing: Graphene and Beyond. *Electronics* 2015, **4**, 651-687.
18. K. Cho, M. Min, T.-Y. Kim, H. Jeong, J. Pak, J.-K. Kim, J. Jang, S. J. Yun, Y. H. Lee, W.-K. Hong and T. Lee, Electrical and Optical Characterization of $MoS_2$ with Sulfur Vacancy Passivation by Treatment with Alkanethiol Molecules. *ACS Nano*, 2015, **9**, 8044-8053.
19. C.-J. Park, H. J. Park, J. Y. Lee, J. Kim, C.-H. Lee and J. Joo, Photovoltaic Field-Effect Transistors Using a $MoS_2$ and Organic Rubrene van der Waals Hybrid. *ACS Appl. Mater. Interfaces*, 2018, **10**, 29848-29856.
20. R. Zhang, D. Drysdale, V. Koutsos and R. Cheung, Controlled Layer Thinning and p-Type Doping of $WSe_2$ by Vapor $XeF_2$. *Adv. Funct. Mater.*, 2017, **27**, 1702455.
21. J. Lee, J. Huang, B. G. Sumpter and M. Yoon, Strain-Engineered Optoelectronic Properties of 2D Transition Metal Dichalcogenide Lateral Heterostructures. *2D Mater*., 2017, **4**, 021016.

22. W. S. Yun, S. W. Han, S. C. Hong, I. G. Kim and J. D. Lee, Thickness and Strain Effects on Electronic Structures of Transition Metal Dichalcogenides: 2H-$MX_2$ Semiconductors (M= Mo, W; X= S, Se, Te). *Phys. Rev. B,* 2012, **85**, 033305.

23. C. Zhou, Y. Zhao, S. Raju, Y. Wang, Z. Lin, M. Chan and Y. Chai, Carrier Type Control of $WSe_2$ Field-Effect Transistors by Thickness Modulation and $MoO_3$ Layer Doping. *Adv. Funct. Mater.,* 2016, **26**, 4223-4230.

24. D. Kiriya, M. Tosun, P. Zhao, J. S. Kang and A. Javey, Air-Stable Surface Charge Transfer Doping of $MoS_2$ by Benzyl Viologen. *J. Am. Chem. Soc.,* 2014, **136**, 7853-7856.

25. P. R. Pudasaini, A. Oyedele, C. Zhang, M. G. Stanford, N. Cross, A. T. Wong, A. N. Hoffman, K. Xiao, G. Duscher, D. G. Mandrus, T. Z. Ward and P. D. Rack, High-Performance Multilayer $WSe_2$ Field-Effect Transistors with Carrier Type Control. *Nano Res.,* 2018, **11**, 722-730.

26. N. Huo, S. Tongay, W. Guo, R. Li, C. Fan, F. Lu, J. Yang, B. Li, Y. Li and Z. Wei, Novel Optical and Electrical Transport Properties in Atomically Thin $WSe_2$/$MoS_2$ p–n Heterostructures. *Adv. Electron. Mater.,* 2015, **1**, 1400066.

27. X. Cui, G.-H. Lee, Y. D. Kim, G. Arefe, P. Y. Huang, C.-H. Lee, D. A. Chenet, X. Zhang, L. Wang, F. Ye, F. Pizzocchero, B. S. Jessen, K. Watanabe, T. Taniguchi, D. A. Muller, T. Low, P. Kim and J. Hone, Multi-Terminal Transport Measurements of $MoS_2$ Using a van der

Waals Heterostructure Device Platform. *Nat. Nanotechnol.*, 2015, **10**, 534-540.

28. R. C. Walker, T. Shi, E. C. Silva, I. Jovanovic and J. A. Robinson, Radiation Effects on Two-Dimensional Materials. *Phys. Status. Solidi. A*, 2016, **213**, 3065-3077.
29. T.-Y. Kim, K. Cho, W. Park, J. Park, Y. Song, S. Hong, W.-K. Hong and T. Lee, Irradiation Effects of High-Energy Proton Beams on $MoS_2$ Field Effect Transistors. *ACS Nano*, 2014, **8**, 2774-2781.
30. F. Giubileo, L. Iemmo, M. Passacantando, F. Urban, G. Luongo, L. Sun, G. Amato, E. Enrico and A. Di Bartolomeo, Effect of Electron Irradiation on the Transport and Field Emission Properties of Few-Layer $MoS_2$ Field-Effect Transistors. *J. Phys. Chem. C*, 2018, **123**, 1454-1461.
31. S. Bertolazzi, S. Bonacchi, G. Nan, A. Pershin, D. Beljonne and P. Samorì, Engineering Chemically Active Defects in Monolayer $MoS_2$ Transistors via Ion-Beam Irradiation and Their Healing via Vapor Deposition of Alkanethiols. *Adv. Mater.*, 2017, **29**, 1606760.
32. M. G. Stanford, P. R. Pudasaini, A. Belianinov, N. Cross, J. H. Noh, M. R. Koehler, D. G. Mandrus, G. Duscher, A. J. Rondinone, I. N. Ivanov, Focused Helium-Ion Beam Irradiation Effects on Electrical Transport Properties of Few-Layer $WSe_2$: Enabling Nanoscale Direct Write Homo-Junctions. *Sci. Rep.* 2016, **6**. 27276.
33. D. Kim, H. Du, T. Kim, S. Shin, S. Kim, M. Song, C. Lee, J. Lee, H. Cheong, D. H. Seo and S. Seo, The Enhanced Low Resistance

Contacts and Boosted Mobility in Two-Dimensional p-type $WSe_2$ Transistors through $Ar^+$ Ion-Beam Generated Surface Defects. *AIP Adv.*, 2016, **6**, 105307.

34. T. Shi, R. C. Walker, I. Jovanovic and J. A. Robinson, Effects of Energetic Ion Irradiation on $WSe_2$/SiC Heterostructures. *Sci. Rep.*, 2017, **7**, 4151.
35. G. Moody, K. Tran, X. Lu, T. Autry, J. M. Fraser, R. P. Mirin, L. Yang, X. Li and K. L. Silverman, Microsecond Valley Lifetime of Defect-Bound Excitons in Monolayer $WSe_2$. *Phys. Rev. Lett.*, 2018, **121**, 057403.
36. S. Das and J. Appenzeller, $WSe_2$ Field Effect Transistors with Enhanced Ambipolar Characteristics. *Appl. Phys. Lett.*, 2013, **103**, 103501.
37. Z. Wang, Q. Li, Y. Chen, B. Cui, Y. Li, F. Besenbacher and M. Dong, The Ambipolar Transport Behavior of $WSe_2$ Transistors and its Analogue Circuits. *NPG Asia Mater.*, 2018, **10**, 703-712.
38. W. Zhao, Z. Ghorannevis, K. K. Amara, J. R. Pang, M. Toh, X. Zhang, C. Kloc, P. H. Tan and G. Eda, Lattice Dynamics in Mono- and Few-Layer Sheets of $WS_2$ and $WSe_2$. *Nanoscale*, 2013, **5**, 9677-9683.
39. A. Ramasubramaniam, Large Excitonic Effects in Monolayers of Molybdenum and Tungsten Dichalcogenides. *Phys. Rev. B*, 2012, **86**, 115409.

40. V. Podzorov, M. E. Gershenson, C. Kloc, R. Zeis and E. Bucher, High-Mobility Field-Effect Transistors based on Transition Metal Dichalcogenides. *Appl. Phys. Lett.*, 2004, **84**, 3301-3303.

41. P. Tonndorf, R. Schmidt, P. Böttger, X. Zhang, J. Börner, A. Liebig, M. Albrecht, C. Kloc, O. Gordan, D. R. Zahn, S. M. de Vasconcellos and R. Bratschitsch, Photoluminescence Emission and Raman Response of Monolayer $MoS_2$, $MoSe_2$, and $WSe_2$. *Opt. Express*, 2013, **21**, 4908-4916.

42. J. Huang, L. Yang, D. Liu, J. Chen, Q. Fu, Y. Xiong, F. Lin and B. Xiang, Large-Area Synthesis of Monolayer $WSe_2$ on a $SiO_2$/Si Substrate and its Device Applications. *Nanoscale*, 2015, **7**, 4193-4198.

43. G. Salitra, G. Hodes, E. Klein and R. Tenne, Highly Oriented $WSe_2$ Thin Films Prepared by Selenization of Evaporated $WO_3$. *Thin Solid Films*, 1994, **245**, 180-185.

44. H. Fang, C. Battaglia, C. Carraro, S. Nemsak, B. Ozdol, J. S. Kang, H. A. Bechtel, S. B. Desai, F. Kronast, A. A. Unal, G. Conti, C. Conlon, G. K. Palsson, M. C. Martin, A. M. Minor, C. S. Fadley, E. Yablonovitch, R. Maboudian and A. Javey, Strong Interlayer Coupling in van der Waals Heterostructures Built from Single-Layer Chalcogenides. *Proc. Natl. Acad. Sci. U. S. A.*, 2014, **111**, 6198-6202.

45. T. C. Taucher, I. Hehn, O. T. Hofmann, M. Zharnikov and E. Zojer, Understanding Chemical versus Electrostatic Shifts in X-Ray Photoelectron Spectra of Organic Self-Assembled Monolayers. *J. Phys. Chem. C*, 2016, **120**, 3428-3437.

46. L. Q. Zhu, K. Kita, T. Nishimura, K. Nagashio, S. K. Wang and A. Toriumi, Interfacial Dipole at High-k Dielectric/$SiO_2$ Interface: X-Ray Photoelectron Spectroscopy Characteristics. *Jpn. J. Appl. Phys*., 2011, **50**, 031502.
47. C. Claeys and E. Simoen, Radiation Effects in Advanced Semiconductor Materials and Devices, Springer, Berlin, 2013.
48. S. R. Messenger, E. A. Burke, G. P. Summers, M. A. Xapsos, R. J. Walters, E. M. Jackson and B. D. Weaver, Nonionizing Energy Loss (NIEL) for Heavy Ions. *IEEE. Trans. Nucl. Sci.*, 1999, **46**, 1595-1602.
49. J. F. Ziegler, J. P. Biersack and U. Littmark, *The Stopping and Range of Ions in Matter*, Pergamon, New York, 1985.
50. R. C. Hughes, Charge-Carrier Transport Phenomena in Amorphous $SiO_2$: Direct Measurement of the Drift Mobility and Lifetime. *Phys. Rev. Lett.*, 1973, **30**, 1333.
51. T. R. Oldham, *Ionizing Radiation Effects in MOS Oxides*. World Scientific, Singapore, 1999.
52. J. Shin, K. Cho, T.-Y. Kim, J. Pak, J.K. Kim, W. Lee, J. Kim, S. Chung, W.K. Hong, and T. Lee. Dose-dependent effect of proton irradiation on electrical properties of $WSe_2$ ambipolar field effect transistors. *Nanoscale* 2019, **11**, 13961
53. P.R. Pudasaini, *et al.* High-performance multilayer WSe2 field-effect transistors with carrier type control. *Nano Research*, 2018, **11**, 722-730.

# Chapter 3. Proton Irradiation Effects on Mechanochemically Synthesized and Flash-evaporated Hybrid Organic-inorganic Lead Halide Perovskites

## In this chapter…

*A hybrid organic-inorganic halide perovskite is a promising material for developing efficient solar cell devices, with potential applications in space science. In this study, we synthesized methylammonium lead iodide ($MAPbI_3$) perovskites via two methods: mechanochemical synthesis and flash evaporation. We irradiated these perovskites with highly energetic 10-MeV proton-beam doses of $10^{11}$, $10^{12}$, $10^{13}$, and $4 \times 10^{13}$ protons/cm$^2$ and examined the proton irradiation effects on the physical properties of $MAPbI_3$ perovskites. The physical properties of the mechanochemically synthesized $MAPbI_3$ perovskites were not considerably affected after proton irradiation. However, the flash-evaporated $MAPbI_3$ perovskites showed a new peak in X-ray diffraction and an increased fluorescence lifetime in time-resolved photoluminescence under high-dose conditions, indicating considerable changes in their physical properties. This difference in behavior*

*between $MAPbI_3$ perovskites synthesized via the abovementioned two methods may be attributed to differences in radiation hardness associated with the bonding strength of the constituents, particularly Pb–I bonds. Our study will help to understand the radiation effect of proton beams on organometallic halide perovskite materials.*

## 3.1. Introduction

Organic-inorganic hybrid halide perovskites (OIHPs) have promising applications in optoelectronic and electronic devices, including solar cells, light-emitting diodes, lasers, photodetectors, and transistor [1-12], owing to their attractive properties, such as high power-conversion efficiency, large charge-carrier diffusion length, large absorption coefficient, and tunable direct bandgap [13,14]. However, the stability of hybrid perovskites needs to be investigated under ambient and harsh environmental conditions to demonstrate their practical applicability. In particular, given the prospect of high-efficiency perovskite solar cells being used in space environments, some researchers have studied the radiation tolerance of perovskite materials and devices to high-energy particles, such as cosmic rays, under space environments. For example, Lang et al. investigated the radiation hardness of inverted methylammonium lead iodide ($MAPbI_3$) perovskite solar cells and found that these devices could tolerate 68-MeV proton-beam doses up to $10^{12}$ protons/cm$^2$ [15]. Miyazawa et al. found that lead halide perovskite solar cells could tolerate proton irradiation dose up to $10^{15}$ particles/cm$^2$ with 50-keV proton

beam which enable to implant proton particles within the perovskite layer causing lattice deformation [16]. However, the effect of isolating perovskites from the influences of other layers of the devices or interfaces that may affect the radiation hardness has not been adequately reported. Lang et al. irradiated lead halide perovskite/copper indium gallium selenide (CIGS) and perovskite/silicon tandem solar cells and attributed most of the device efficiency losses to the CIGS and silicon layers and not the perovskite layer [17]. Therefore, exclusive research to investigate the apparent radiation hardness of the perovskite layer itself is necessary to avoid the influence of other surrounding layers.

In this study, we synthesized organic-inorganic hybrid $MAPbI_3$ perovskites via two methods: mechanochemical synthesis and flash evaporation. Then, we investigated the effects of irradiation on the physical properties of $MAPbI_3$ perovskites under various high-energy proton-beam doses. For this purpose, the physical properties of perovskites synthesized via two methods were characterized systematically before and after 10-MeV proton beam irradiation doses of $10^{11}$, $10^{12}$, $10^{13}$, and $4 \times 10^{13}$ protons/cm$^2$ using X-ray diffraction (XRD), ultraviolet-visible (UV-Vis) absorbance spectroscopy, and photoluminescence. Mechanochemically synthesized $MAPbI_3$ perovskites did not exhibit considerable changes in their physical properties after the proton irradiations, indicating that this perovskite can tolerate dose conditions in this study. Conversely, flash-evaporated $MAPbI_3$ perovskites exhibited considerable changes in their physical properties after the high-dose proton irradiation. This study aims at broadening our understanding of the radiation tolerance of perovskite under high-energy proton-beam irradiation to estimate the potential of perovskites in space applications.

## 3.2. Experiments

### 3.2.1 Mechanochemical synthesis of $MAPbI_3$ perovskite

$MAPbI_3$ perovskite powder was synthesized mechanochemically, as illustrated in figure 3.1. Figure 3.1 (a) shows an optical image of the precursors 1.59-g methylammonium iodide (MAI) (white powder) and 4.61-g lead iodide ($PbI_2$) (yellow powder), ground using stainless steel balls with diameters of 1.27, 0.95, and 0.63 cm (4, 4, and 60 balls, respectively) in an alumina jar. The molecular structures of MAI and $PbI_2$ are schematically illustrated in figure 3.1 (d). The alumina jar containing the mixture was ball milled at 300 Hz for 5 h (BD4530, LK Lab) (Figure 3.2).

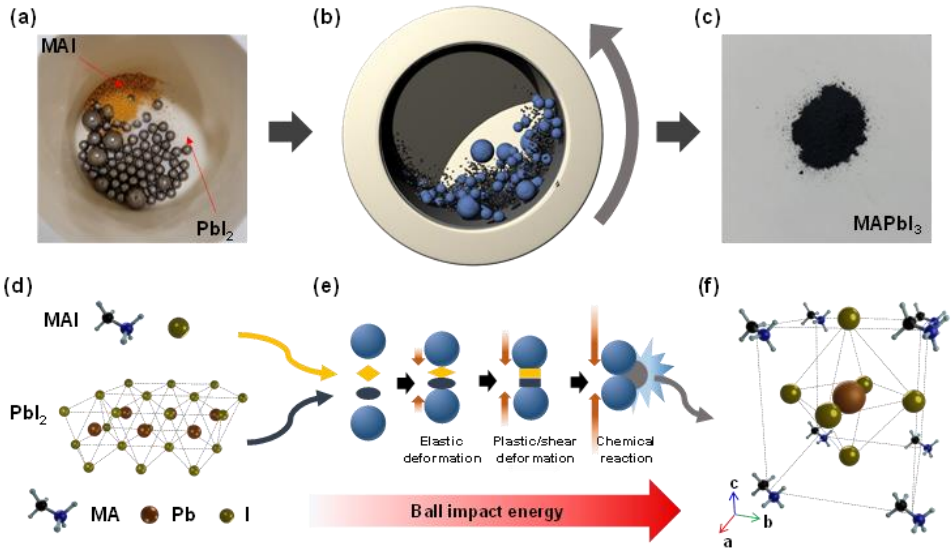


**Figure 3.1** (a) Optical image of methylammonium iodide (MAI) and lead iodide ($PbI_2$) precursor powders in alumina jar. (b) Schematic of mechanochemical synthesis of $MAPbI_3$ perovskite through a ball mill. (c) Optical image of mechanochemically synthesized $MAPbI_3$ perovskite powder. (d) Structures of MAI and $PbI_2$ precursors. (e) Mechanism of mechanochemical reaction from reactants to products via soft ball milling. (f) Structure of $MAPbI_3$ perovskite unit cell. Adapted from Shin *et al.* [52]

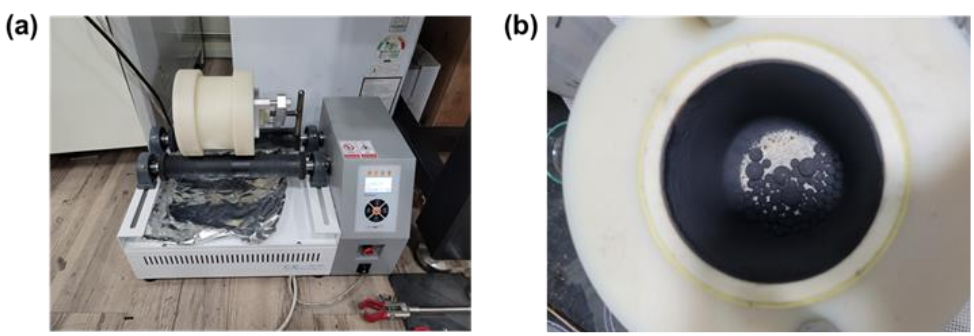


**Figure 3.2** (a) Image of ball mill system. (b) Synthesized perovskite powder.

Adapted from Shin *et al.* [52]

### 3.2.2 Synthesis of $MAPbI_3$ perovskite films via flash evaporation

As, previously reported, $MAPbI_3$ perovskite films were synthesized via a flash evaporation method [18, 19]. First, 500-μm-thick glass substrates were cleaned via sonication in acetone, isopropyl alcohol, and deionized water for 10 min each. Then, the substrates were treated with $O_2$ plasma (30 sccm, 50 W) for 120 s using a reactive ion etcher (RIE; AFS-R4T, AllForSystem). These treated substrates were transferred to a vacuum chamber and placed in a substrate holder 30 cm above a source boat for flash evaporation (**see figure 4(a**)). To deposit $MAPbI_3$ perovskite film, we applied a high current of 100 A to rapidly heat the 650-mg mechanochemically synthesized $MAPbI_3$ powder and 167-mg MAI powder placed in the source boat to evaporate the source powder mixture.

### 3.2.3 Characterization of mechanochemically synthesized perovskite powder and flash evaporated perovskite film

The optical images and energy-dispersive spectra of the synthesized perovskite powder and film samples were acquired via field-emission scanning electron microscopy (FESEM; JSM-7800F Prime, JEOL Ltd). Powder or film XRD spectra were measured using an X-ray diffractometer (SmartLab, Rigaku) in the National Center for Interuniversity Research Facilities of Korea.

Photoluminescence (PL) spectra and time-resolved (Tr) PL spectra were measured using the XperRAM 200 with a laser of 532-nm excitation wavelength and XperRF (Nanobase Inc.) with a pulsed laser that has a 405-nm excitation wavelength, 5000-kHz repetition rate, and 1-μW power, respectively. The absorbance spectra were acquired via UV–Vis spectroscopy (V-770, Jasco).

### 3.2.4 Proton irradiation

We used the MC-50 cyclotron at the Korea Institute of Radiological and Medical Sciences for performing proton beam irradiation experiments. The 10-MeV proton beam irradiation source generated by $2 \times 10^{10}$ protons per second per square centimeter, corresponding to a 10-nA average current had a ~1-cm spot size. Proton irradiation was performed in a vacuum environment. In order to irradiate the proton on the powder samples, the mechanochemically synthesized perovskite powder was placed on 15 μm thick Al foil. 140 mg perovskite powder was put on the Al foil with an area of 1.4 cm × 1.4 cm with a thickness of ~150 μm. The flash-evaporated perovskite film was directly attached to the equipment without any additional packing steps. The perovskite powder and films were irradiated at $10^{11}$, $10^{12}$, $10^{13}$, and $4 \times 10^{13}$ protons/cm$^2$ proton-beam doses, which correspond to irradiation times of 5, 50, 500, and 2000 s, respectively. Cosmic ray proton flux varies depending on distance from earth, and the dose of $4 \times 10^{13}$ protons/cm$^2$ equivalent to the number of protons encountered in space over 10 years [20, 21].

To allow the radioactivity to fall to a safe level, the proton-irradiated samples were retained in the facility for one day after the completion of proton beam irradiation experiments.

## 3.3. Results and discussion

### 3.3.1 Characterization of Mechanochemically synthesized perovskite

We used an electrically rotating ball mill in a so-called “planetary instrument,” a simplified version of which is shown in figure 3.1 (b), among various mechanochemical synthesis methods, such as hand-grinding or automated mixer mill methods. This method facilitates adequate controllability of rotation frequency and grinding force [22]. As the alumina jar rotates, mechanical energy, such as compression, shear, or friction, formed between the stainless balls or between the balls and the jar is transferred to the mixture (figure 3.1 (b) and 3.1 (e)).

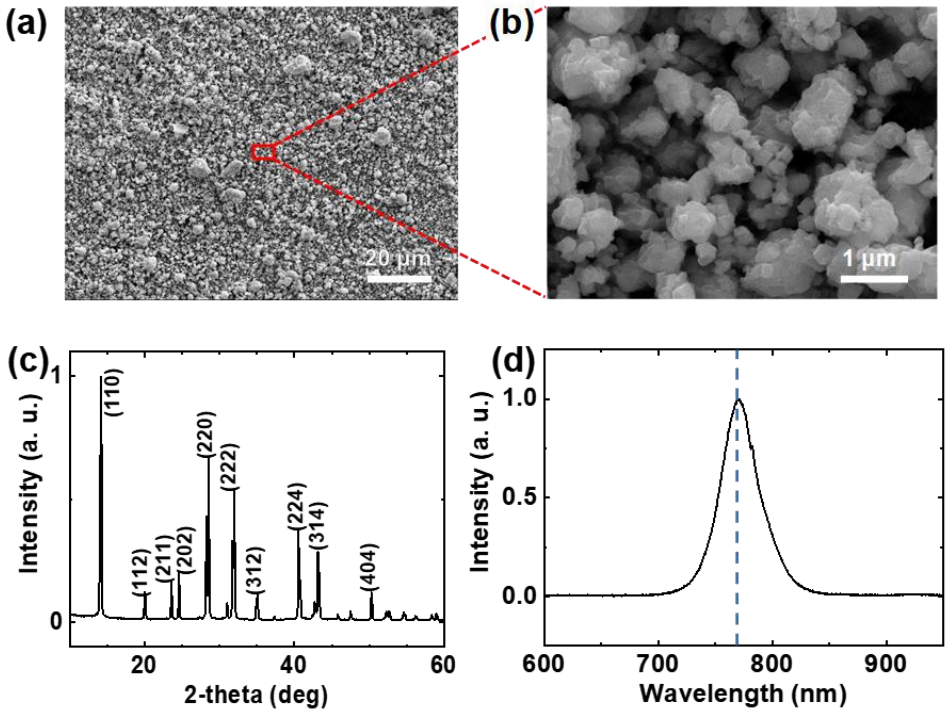


**Figure 3.3** (a, b) SEM images of MCS $MAPbI_3$ perovskite powder. (c) XRD spectrum of MCS $MAPbI_3$ perovskite powder. (d) Steady-state photoluminescence (PL) spectrum of MCS $MAPbI_3$ perovskite powder. Adapted from Shin *et al.* [52]

When sufficient energy is transferred, the chemical reaction occurs, and high-purity perovskite samples can be obtained as a form of dry colloidal powder. This method does not require dissolving reagents, and fresh-reactant surfaces are constantly exposed during the synthesis process [22-24]. Figure 3.1 (c) presents an optical image that shows that the mechanochemically synthesized (denoted as "MCS") $MAPbI_3$ perovskite powder is black as is known. Figure 3.1 (f) shows the crystal structure of the MCS perovskite, which is the tetragonal phase. Note that

flash-evaporated perovskite has the same tetragonal structure [25-27].

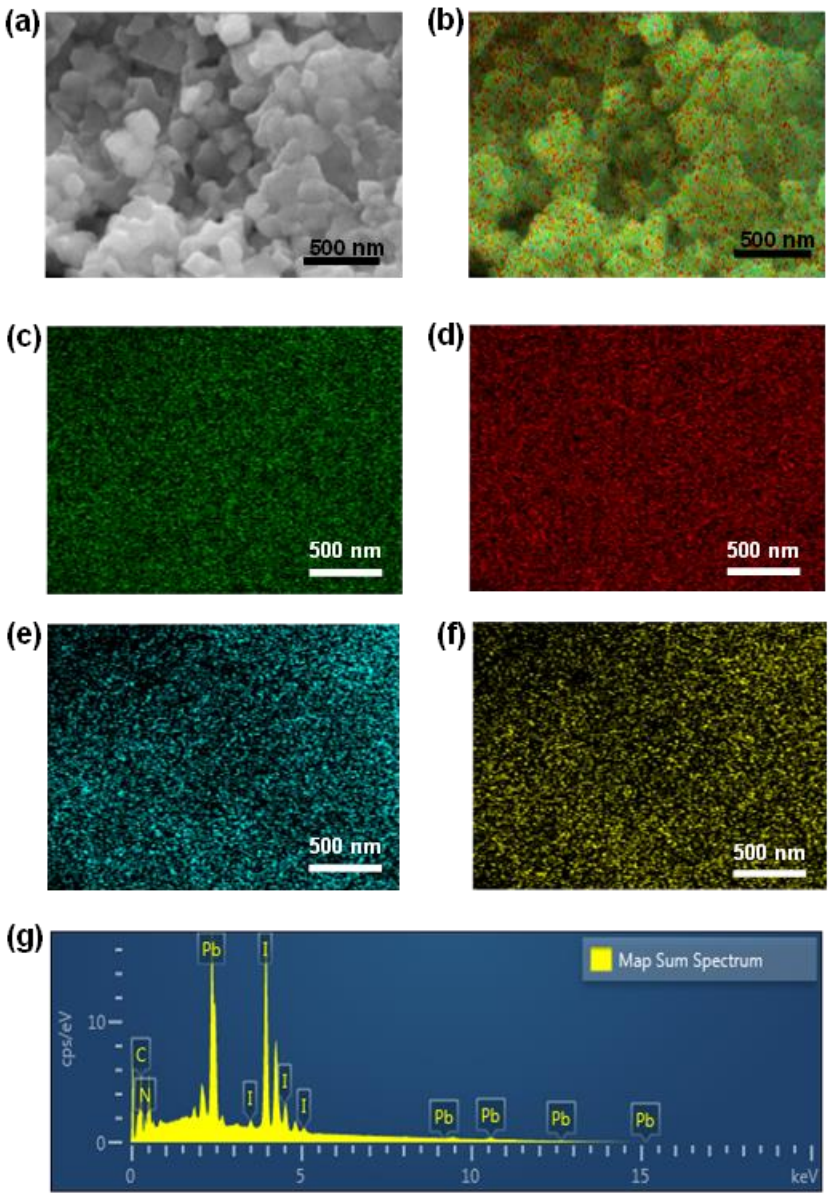


**Figure 3.4** (a) SEM image and (b-f) EDS mapping images of $MAPbI_3$ perovskite powder sample. (b) Combination map of Pb, I, C, and N and map of (c) Pb, (d) I,

(e) C, and (f) N. (g) EDS spectral line pattern of $MAPbI_3$ powder sample. Adapted from Shin *et al.* [52]

To verify whether MCS $MAPbI_3$ perovskite powder was well synthesized, we characterized its elemental composition and structural properties as well as photophysical properties using SEM, energy-dispersive X-ray spectroscopy (EDS), powder XRD, and PL. Figures 3.3 (a) and 3.3 (b) show the SEM images of the MCS $MAPbI_3$ perovskite powder with a particle size of tens to hundreds of nanometers. Uniform spatial distributions of elements such as C, Pb, and I were confirmed via EDS results (supplementary figure 3.4). The powder XRD peaks indicated that the MCS perovskite powder have a lattice structure of $MAPbI_3$ perovskite phase without remaining precursor $PbI_2$ that did not participate in the reaction (figure 3.3 (c)) [28, 29]. Figure 3.3 (d) shows a PL peak at ~770 nm from the steady-state PL emission with an excitation source of 532 nm, which corresponds to the known ~1.6-eV bandgap value of the MCS $MAPbI_3$ perovskite powder [28, 30]. Based on these experimental results, we confirmed that the MCS $MAPbI_3$ perovskite powder was successfully synthesized.

### 3.3.2 Proton irradiation hardness of MCS perovskite

Then, the MCS $MAPbI_3$ perovskite powder was irradiated by 10-MeV proton beams under irradiation doses of $10^{11}$, $10^{12}$, $10^{13}$, and $4 \times 10^{13}$ protons/cm$^2$,

respectively. We compared the physical properties of MCS $MAPbI_3$ perovskite

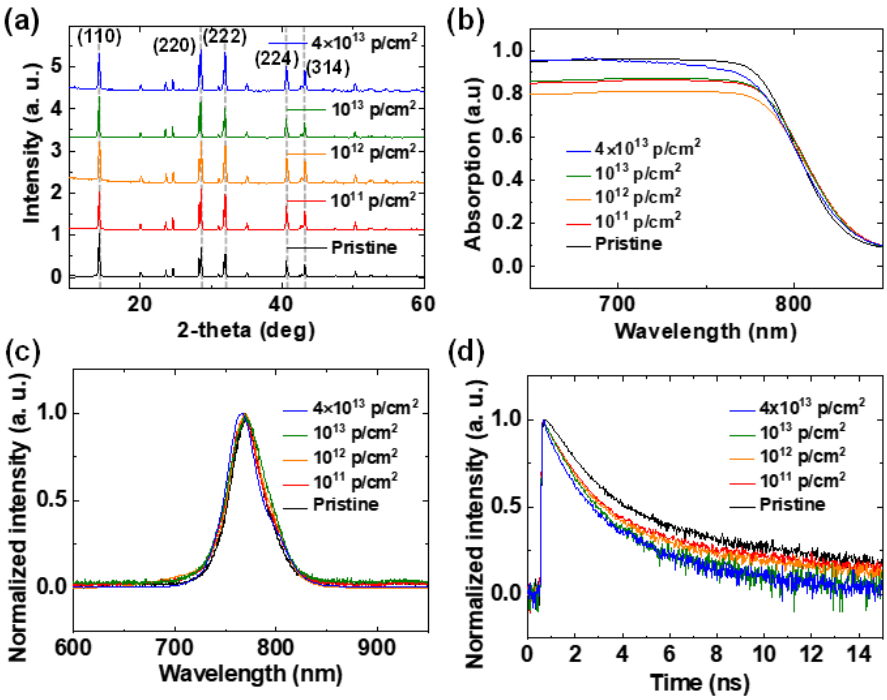


**Figure 3.5** (a) XRD, (b) UV-Vis absorbance, (c) PL, and (d) TRPL spectra of MCS $MAPbI_3$ perovskite powder samples before and after proton irradiation at doses of $10^{11}$, $10^{12}$, $10^{13}$, and $4 \times 10^{13}$ protons/cm$^2$. Adapted from Shin *et al.* [52]

powder systematically before and after proton irradiation to investigate the effects of proton irradiation. Figure 3.5 (a) shows the XRD spectra of the MCS $MAPbI_3$ perovskite powder before proton irradiation (denoted as "pristine") and after various proton irradiation doses. The XRD spectra did not indicate any considerable changes before and after proton irradiation, which suggests that the proton beam irradiation did not considerably affect the MCS $MAPbI_3$ perovskite

powder. Furthermore, no conspicuous changes beyond the measurement error range were observed in the UV-Vis absorbance (figure 3.5 (b)) and PL results (figure 3.5 (c)) of the MCS $MAPbI_3$ perovskite powder before and after proton irradiation although PL spectra seem to have slight variation in the peak width. Note that the PL spectra were the average values of point-scanned PL at four to five different positions and normalized because the intensity varies according to the location of the powder sample.

The MCS $MAPbI_3$ perovskite powder was also characterized by TRPL, which has proven to be a reliable and suitable tool for extracting minority-carrier lifetimes [31-33]. Figure 3.5 (d) shows TRPL decay curves with excitation pulse laser of 405 nm wavelength and 5000 kHz repetition rate for the MCS $MAPbI_3$ perovskite powder. We analyzed these curves according to the following equation [34, 35]:

$$I(t) = a_1 e^{-t/\tau_1} + a_2 e^{-t/\tau_2} + b, \quad (1)$$

where a and $\tau$ are the amplitude and fluorescence lifetimes of the TRPL decay curve, respectively, and b is a fitting parameter. The subscripts 1 and 2 represent early- and late-stage recombination processes, respectively. The detailed fitting results are provided in figures 3.6, 3.7 (a) and table 3.1.

Particularly, we found that both the $\tau_1$ and $\tau_2$ decreased with increasing irradiation dose. For the pristine case, $\tau_1$ was found to be ~3.53 ns, which

decreased from ~2.78 to ~2.15 ns for dose from $10^{11}$ to $4 \times 10^{13}$ protons/cm$^2$. Similarly, $\tau_2$ was found to be ~28.4 ns for the pristine case, which decreased from ~25.0 to ~7.82 ns for dose from $10^{11}$ to $4 \times 10^{13}$ protons/cm$^2$. In other words, higher

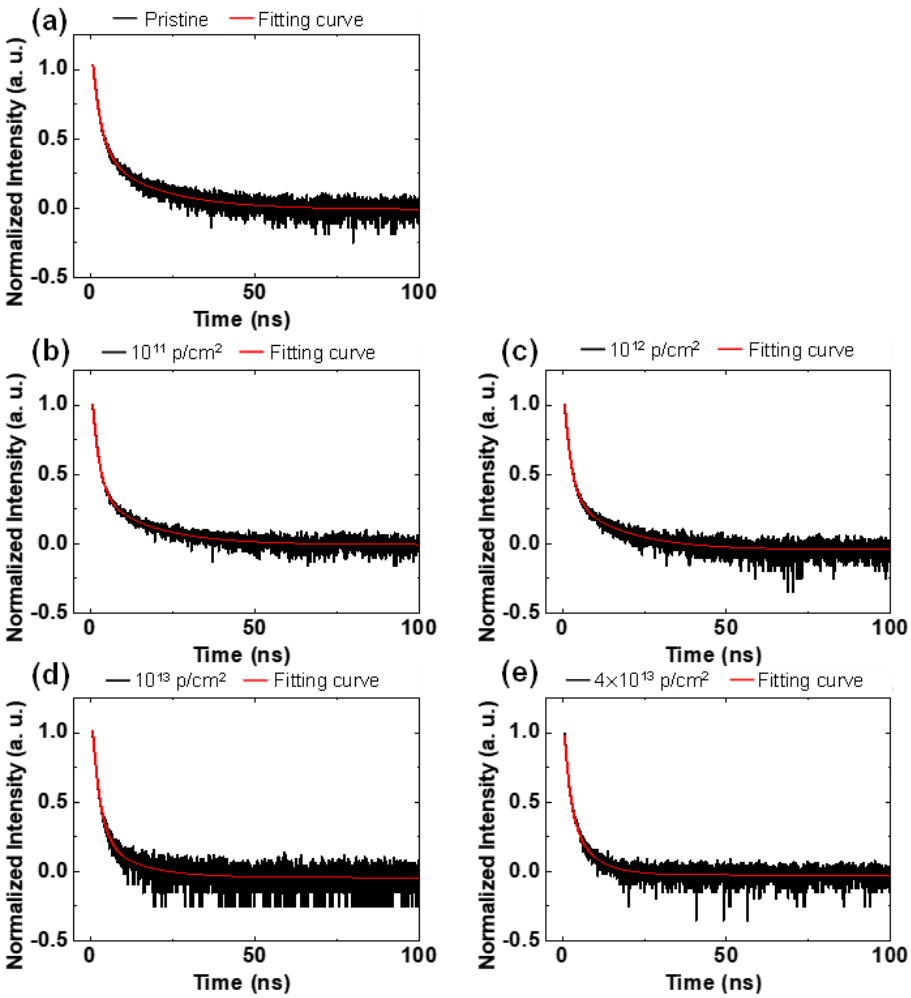


**Figure 3.6** TRPL spectra and fitting curves of $MAPbI_3$ perovskite powder samples of (a) before irradiation and (b-e) after proton irradiation under dose conditions of (b) $10^{11}$, (c) $10^{12}$, (d) $10^{13}$, and (e) $4\times 10^{13}$ protons/cm$^2$. The fitting parameters of $\tau_1$ and $\tau_2$ are in the unit of ns. Adapted from Shin *et al.* [52]

dose irradiation of the samples more accelerated the recombination process (i.e., τ values decreased). Overall, the results presented in figure 3 indicate that the proton irradiation did not cause considerable structural changes in the MCS $MAPbI_3$ perovskite powder (figures 3.5 (a)-3.5 (c)); however, it accelerated the recombination process. This finding suggests that the proton beams might generate

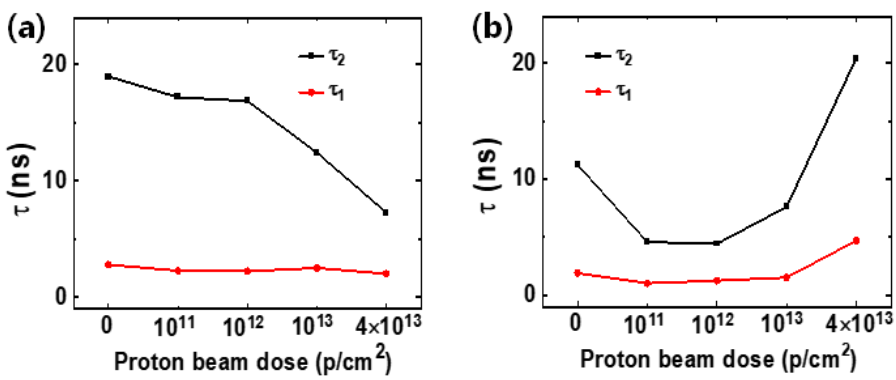


**Figure 3.7** Fluorescence lifetimes ($\tau_1$, $\tau_2$) as a function of proton beam dose for (a) MCS and (b) flash evaporated perovskites. Adapted from Shin *et al.* [52]

**Table 3.1** The fluorescence lifetime of TRPL fitted to Equation (1) in the original manuscript. Adapted from Shin *et al.* [52]

| Dose (protons/cm$^2$) | MCS | | Flash evaporation | |
|---|---|---|---|---|
| | $\tau_1$ (ns) | $\tau_2$ (ns) | $\tau_1$ (ns) | $\tau_2$ (ns) |
| Pristine | 2.80 | 18.98 | 1.91 | 11.23 |
| $10^{11}$ | 2.28 | 17.19 | 1.04 | 4.59 |
| $10^{12}$ | 2.24 | 16.86 | 1.27 | 4.44 |
| $10^{13}$ | 2.52 | 12.43 | 1.53 | 7.63 |
| $4 \times 10^{13}$ | 2.02 | 7.27 | 4.71 | 20.44 |

shallow traps that can allow trap-mediated recombination (figure 3.5 (d)). A detailed discussion of this point is offered later. We also measured EDS after proton irradiation under dose of $4 \times 10^{13}$ proton/cm$^2$ (figure 3.8). In our results, no noticeable change in composition was observed between before and after proton irradiation on MCS perovskite powder, considering the measurement error range of the system.

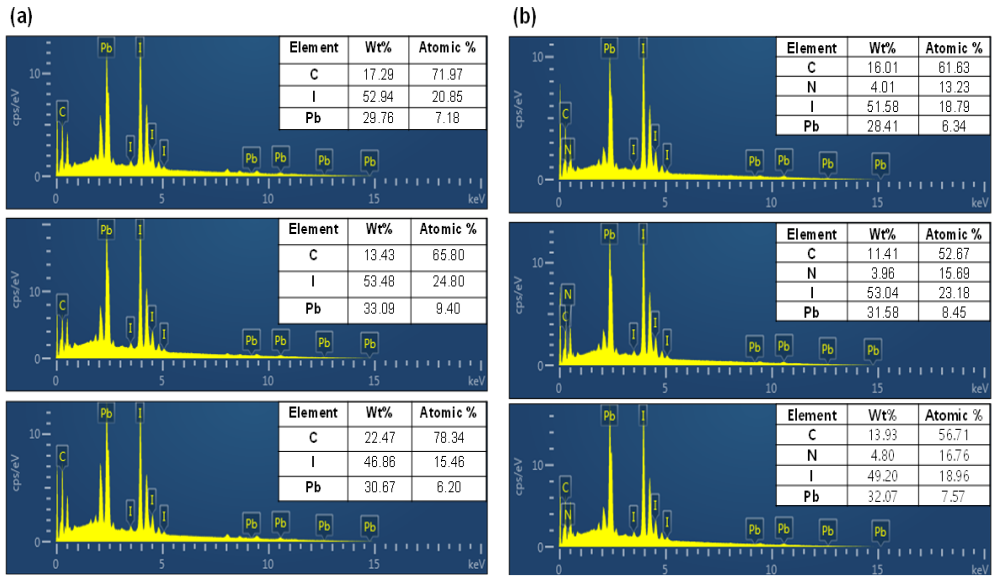


**Figure 3.8** EDS results of MCS perovskite powder (a) before and (b) after irradiation under dose of $4 \times 10^{13}$ proton/cm$^2$. Adapted from Shin *et al.* [52]

### 3.3.3 Proton hardness of flash-evaporated perovskite

We synthesized $MAPbI_3$ perovskite films via flash-evaporation and investigated the proton irradiation effect. The flash evaporation process is schematically illustrated in figure 3.9 (a). Detailed information regarding flash evaporation is provided in the Experimental section. This flash evaporation method offers the advantages of rapid, solvent-free deposition for a large-scale production of OIHP films [18, 36]. The flash-evaporated $MAPbI_3$ perovskite film in this study was ~150-nm-thick with a grain size of tens to hundreds of nanometers (figure 3.9 (b) and figure 3.10).

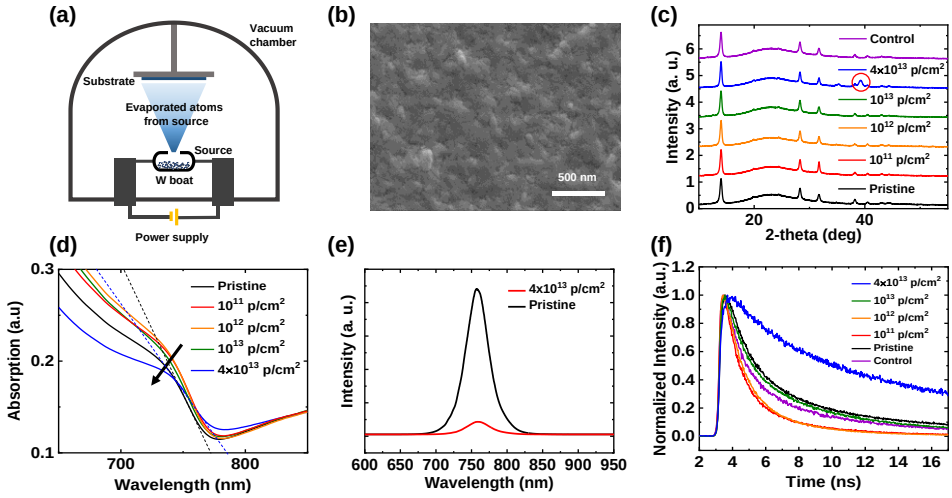


**Figure 3.9** (a) Schematic of $MAPbI_3$ perovskite film deposition by flash evaporation. (b) SEM image of flash-evaporated $MAPbI_3$ perovskite film. (c) XRD, (d) UV-Vis absorbance, (e) PL, and (f) TRPL spectra of flash-evaporated $MAPbI_3$ perovskite film samples before and after proton irradiation. Adapted from Shin *et al.* [52]

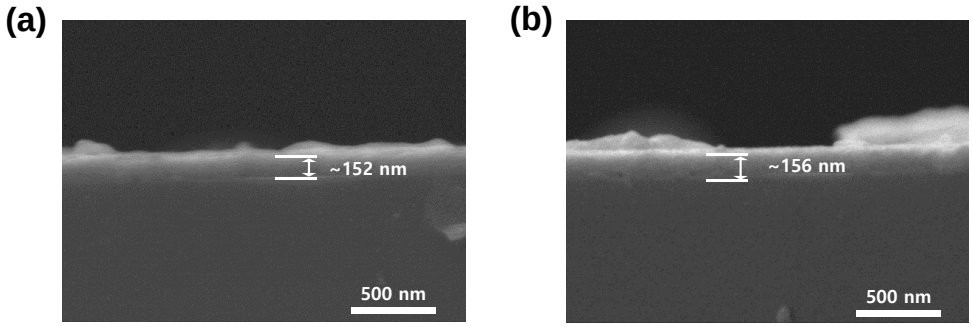


**Figure 3.10** Cross-sectional SEM of flash evaporated perovskite films. Adapted from Shin *et al.* [52]

Similarly, the physical properties of flash-evaporated $MAPbI_3$ perovskite films were characterized using XRD, UV-Vis absorbance, PL, and TRPL before and after proton irradiation. Figure 3.9 (c) shows the XRD spectra of flash-evaporated perovskite film before and after proton irradiation. In this figure, the "pristine" and "control" curves represent the XRD spectra of the sample before proton irradiation, and that of the same pristine sample stored with other proton-irradiated samples under the same conditions, respectively. Note that all the samples were stored in a desiccator whose pressure was maintained at approximately 1 torr during travel between the laboratory and proton irradiation facility. Similar to the XRD spectra for the MCS $MAPbI_3$ perovskite powder (figure 3.3 (c) and figure 3.5 (a)), the XRD spectrum for the pristine $MAPbI_3$ perovskite film shows the peaks corresponding to the well-synthesized $MAPbI_3$ perovskite lattice structure (figure 3.9 (c)), with broader XRD peak width than MCS powder, because the average grain size of flash-evaporated film (~17.12 nm) is smaller than MCS powder (~34.89 nm) which is obtained by the Scherrer equation [37]. It is noteworthy that the 2-theta value for the peaks corresponding to the flash–evaporated $MAPbI_3$ perovskite film decreased by ~0.1° compared with those of the MCS $MAPbI_3$ perovskite powder samples (figure 3.11).

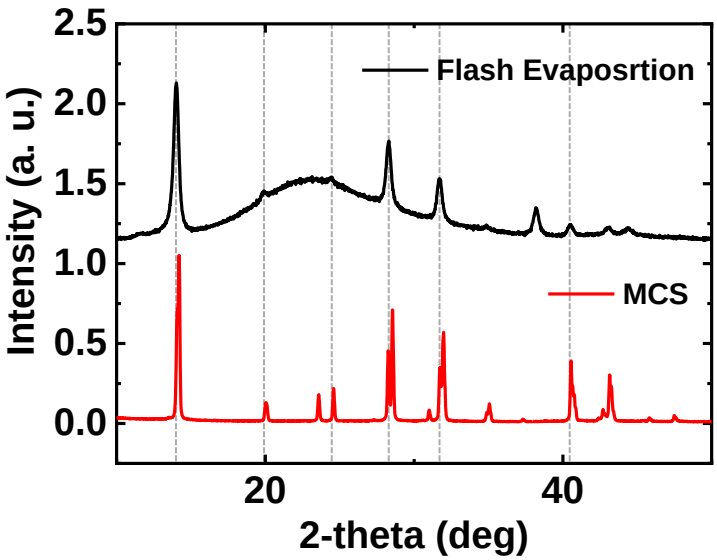


**Figure 3.11** XRD of pristine perovskites synthesized by MCS and flash evaporation. Adapted from Shin *et al.* [52]

This change may suggest that the MCS $MAPbI_3$ powder possesses a $PbI_6$ framework of superior compactness [25] with a less defective nature [38, 39] than that of the flash-evaporated $MAPbI_3$ film. The defect in iodide, which is significantly related to the stability of the perovskite, locally increases the electrostatic repulsion of lead cations in $PbI_6$ framework, thereby increasing the lattice size [25]. The broad peak around 25° can be attributed to the glass substrate.

It is noteworthy that low-dose ($10^{11}$, $10^{12}$, and $10^{13}$ protons/cm$^2$) proton irradiation did not considerably affect the XRD spectra of the flash–evaporated $MAPbI_3$ perovskite films whereas high-dose ($4 \times 10^{13}$ protons/cm$^2$) proton irradiation produced a new peak around 39.2° (red circled in figure 3.9 (c)), which

indicates the presence of $PbI_2$ impurity generated via a high-dose proton irradiation in our samples[40].

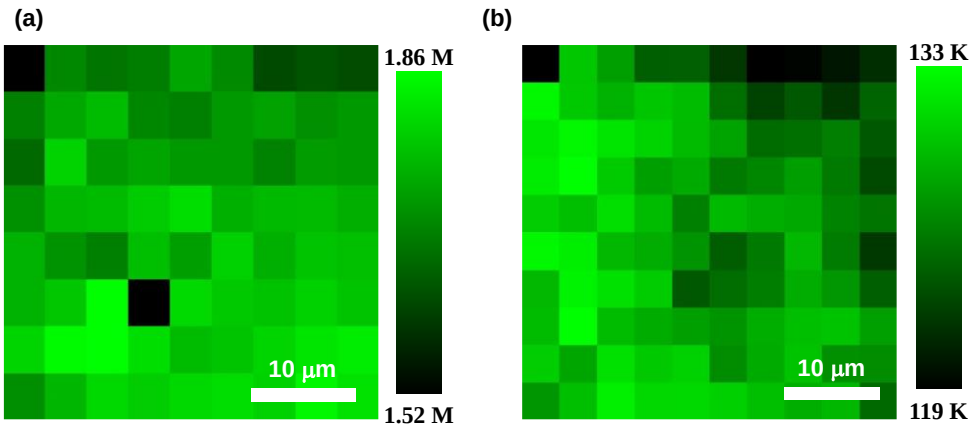


**Figure 3.12** Areal PL mapping of flash-evaporated perovskite films for (a) before and (b) after proton irradiation of $4 \times 10^{13}$ proton/cm$^2$. PL area mapping performed using a 1 μW power laser with a wavelength of 532 nm for 500 ms per point. We scanned area of $32 \times 36$ μm$^2$ and $40 \times 40$ μm$^2$ for the samples before the irradiation and after the irradiation, respectively, with a pixel spacing of 4 μm to prevent the overlapping laser cross-section. Adapted from Shin *et al.* [52]

Figures 3.9 (d)-3.9 (f) show the UV-Vis absorbance, PL, and TRPL data for the flash evaporated perovskite films before and after the proton irradiation. As shown in figure 3.9 (d), the absorbance onset position did not change much for all irradiation conditions, but the slope of the spectrum below ~750 nm became smaller after the proton irradiation of high dose condition of $4 \times 10^{13}$ proton/cm$^2$.

Such change can also be associated with the slight deformation of $MAPbI_3$ which introduces additional trap sites in the bandgap, as previously reported[41]. The absorbance onset in the ~770-nm flash-evaporated $MAPbI_3$ perovskite films differed from that of the ~820-nm MCS $MAPbI_3$ perovskite powder samples (figures 3.5 (b) and figure 3.9 (d)). This disparity suggests smaller bandgap of MCS $MAPbI_3$ perovskite powders, which is associated with the less defects nature and superior compactness $PbI_6$ framework [25].

Figure 3.9 (e) shows the PL data for the flash-evaporated $MAPbI_3$ perovskite film before (pristine) and after proton irradiation at the highest dose ($4 \times 10^{13}$ protons/cm$^2$). Note that the PL spectra of the flash-evaporated film are the average values of area scan (figure 3.12). The PL peak positions did not differ but the intensity decreased by approximately 90% after high-dose ($4 \times 10^{13}$ protons/cm$^2$) proton irradiation compared with that of the pristine sample. This can be attributed to the generated deep traps, which act as nonradiative recombination centers because the shallow traps such as Pb vacancies and MA interstitials, which are majority traps with the lowest defect formation energy in $MAPbI_3$ perovskite, do not act as non-radioactive recombination centers unlike deep defects [42, 43]. Notably, unlike the normalized PL spectra of the powder samples (figure 3.5 (c)), the PL spectra of the flash-evaporated $MAPbI_3$ perovskite films are not normalized because the intensity does not vary according to the location of the uniform film sample. Thus, the intensity comparison is meaningful. The PL peak position for the ~760-nm flash-evaporated $MAPbI_3$ perovskite films differed slightly from that of the ~770-nm of the MCS $MAPbI_3$ perovskite powder samples (figure 3.5 (c) and figure 3.9 (e)). This disparity is consistent with the trend in absorbance data

between the two sample types (figure 3.5 (b) and figure 3.9 (d)).

Figure 3.9 (f) shows the TRPL data for the flash-evaporated $MAPbI_3$ perovskite films analyzed using equation (1). As the proton-irradiation dose increased, the τ

values were found to decrease relative to the pristine sample and then increase

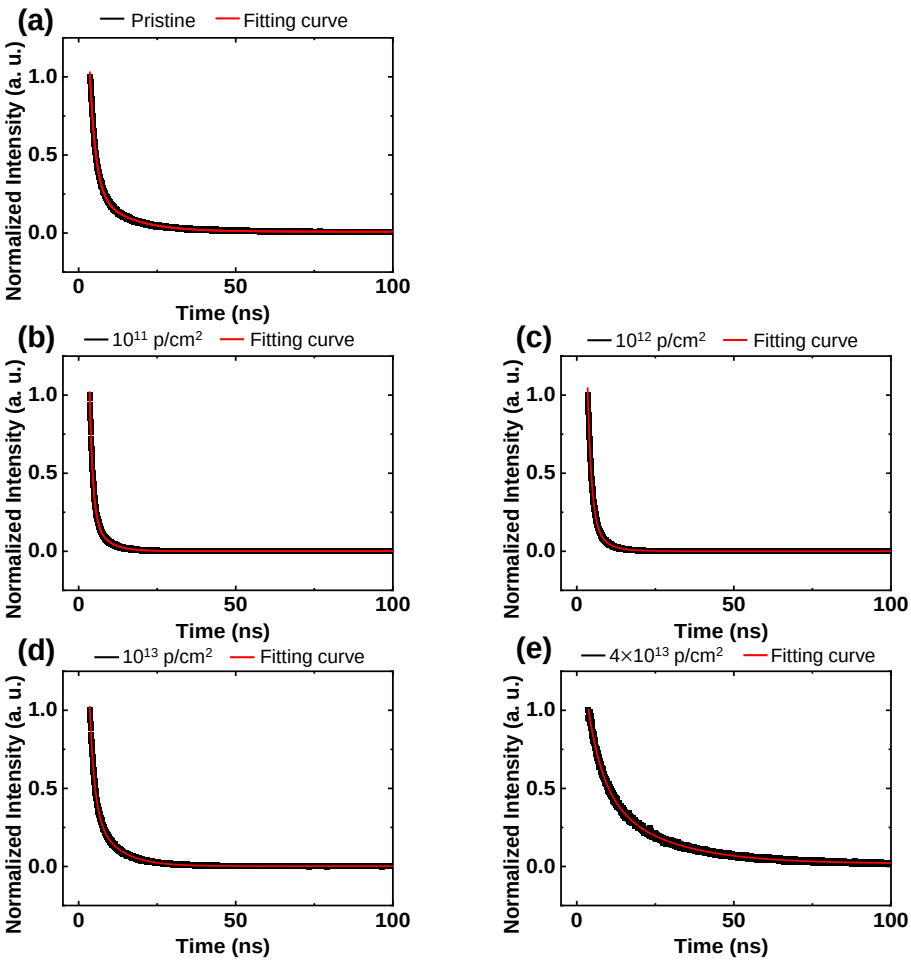


**Figure 3.13** TRPL spectra and fitting curves of $MAPbI_3$ perovskite films of (a) before irradiation and (b-e) after proton irradiation under dose conditions of (b)

$10^{11}$, (c) $10^{12}$, (d) $10^{13}$, and (e) $4\times 10^{13}$ protons/cm. The fitting parameters of $\tau_1$ and $\tau_2$ are in the unit of ns. Adapted from Shin *et al.* [52]

**Table 3.2** Coefficient of variations of fluorescence lifetime. Adapted from Shin *et al.* [52]

| | MCS | | Flash evaporation | |
|---|---|---|---|---|
| | $\tau_1$ (ns) | $\tau_2$ (ns) | $\tau_1$ (ns) | $\tau_2$ (ns) |
| Coefficient of variations | 0.11 | 0.29 | 0.64 | 0.61 |

(figures 3.13, 3.7 (b) and table 3.1). Particularly, $\tau_1$ was ~1.91 ns for the pristine case, which decreased to ~1.04 ns at dose of $10^{11}$ protons/cm$^2$ and increased from ~1.27 to ~4.71 ns at doses from $10^{12}$ to $4 \times 10^{13}$ protons/cm$^2$, respectively. Similarly, $\tau_2$ was ~11.23 ns for the pristine case, which decreased to ~4.59 and ~4.44 ns at doses of $10^{11}$ and $10^{12}$ protons/cm$^2$ and increased to 7.63 and 20.44 ns at doses of $10^{13}$ and $4 \times 10^{13}$ protons/cm$^2$, respectively. These results imply that the recombination process was accelerated when the samples were irradiated at low doses because of the generation of shallow traps. Conversely, the recombination process became slow when the samples were irradiated at high doses because of the generation of deep traps. Note that we obtained the coefficients of variations of fluorescence lifetime (table 3.2) to see the degree of variability. According to this,

the variation in $\tau_2$ is similar to that of $\tau_1$. Also we conducted the EDS after proton irradiation for the flash-evaporated perovskite film under a dose of $4 \times 10^{13}$ proton/cm$^2$ (figure 3.14). Similar to the MCS perovskite sample, a noticeable change in composition after proton irradiation was not observed.

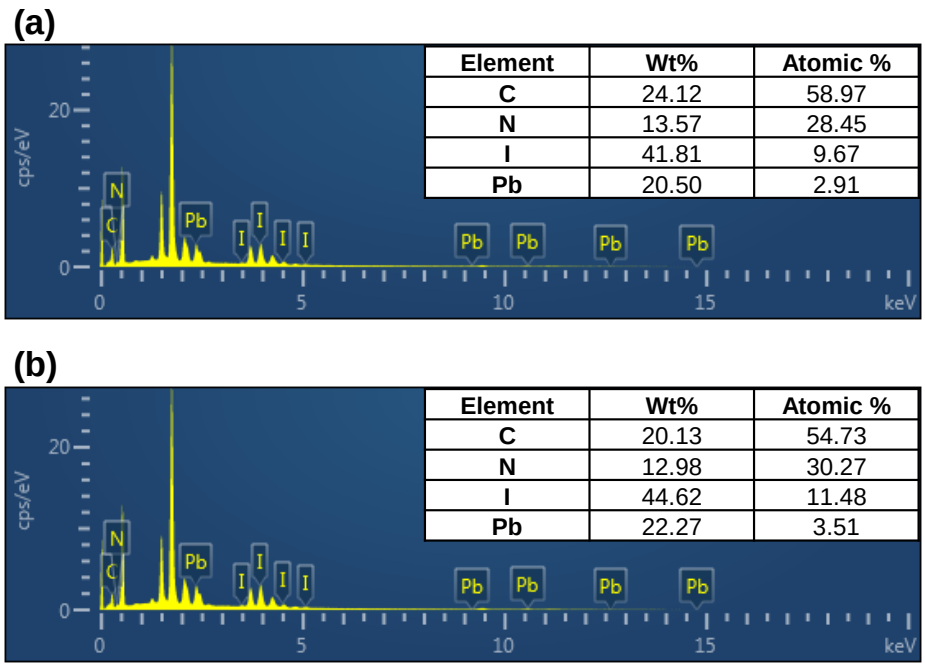


**Figure 3.14** EDS results of flash-evaporated perovskite film (a) before and (b) after irradiation under dose of $4 \times 10^{13}$ proton/cm$^2$. Adapted from Shin *et al.* [52]

### 3.3.4 SRIM results and proton matter interaction

Figure 3.15 (a) shows the energy-loss depth profiles of a 10-MeV proton beam based on the simulation results performed using Stopping and Range of Ions in

Matter (SRIM) software, which is a computer program that calculates the interactions of energetic ions with target matter.

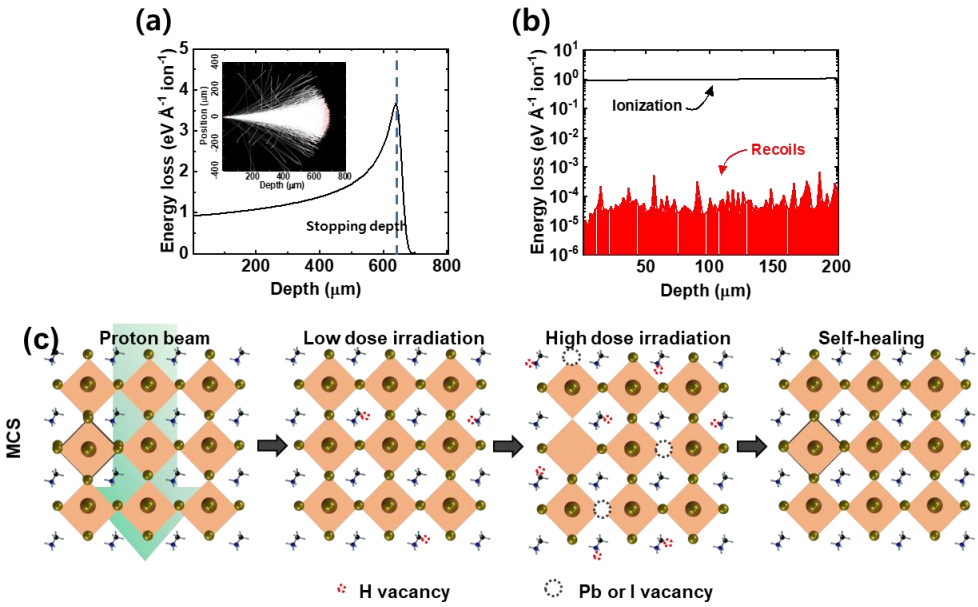


**Figure 3.15** Energy loss profiles of protons simulated via SRIM (a) in the full range and (b) in the range of 0–200 μm. (c) Schematics depicting the effects of proton beam irradiation on perovskite. Left image shows schematic for pristine perovskite, two images in the middle show schematics for perovskite irradiated under a low dose (left middle), in which the effect of hydrogen vacancies is dominant, and a high dose (right middle), in which the effects of lead and iodide vacancies increase. Right image shows schematic of self-healed perovskite in which hydrogen atoms released from bonds reassume their proper lattice positions. Adapted from Shin *et al.* [52]

There are two main processes in which a high-energy proton beam loses its energy. First, the high-energy protons are slowed down during the electronic stopping process, losing some energy and creating electron-hole pairs. Then, after the protons sufficiently slow down, they lose most of the energy during the nuclear stopping process and stop near the stopping depth, damaging the lattice of the target material [44-47]. Therefore, knowing the thickness of the target material compared with the stopping depth is necessary. According to the SRIM simulation results, as shown in figure 3.15 (a), most protons have a stopping depth near 650 μm, which greatly exceeds the thickness of the perovskite samples (150 μm of MCS $MAPbI_3$ perovskite powder samples or 150 nm of flash-evaporated $MAPbI_3$ perovskite film samples). Most protons would pass through the samples while transferring energy via the ionization process in the material, creating homogeneous defects throughout the entire perovskite material (figure 3.15 (b)).

When the proton beam irradiates perovskite, it can create electron-hole pairs along the irradiation path and break the bonds in the perovskite material. In this case, covalent bonds in the organic cation part (i.e., methylammonium, $CH_3$–$NH_3^+$), such as the C–H and N–H bonds, are vulnerable to protons because they have low bonding energy (left middle image of figure 3.15 (c)). However, these broken-bond defects comprising mainly hydrogen vacancies in place of these bonds do not significantly degrade the material, because the wandering hydrogen atoms that come off the bonds have high mobility so they can take the proper lattice position, which is called as 'self-healing' process (right image of figure 3.15 (c)) [15, 48-51]. As the proton irradiation dose increases, constituent atoms of high

bonding energy (i.e., Pb or I atoms in the $PbI_6$ framework) detach and remain as defects rather than relax back to their lattice positions (right middle image of figure 3.15 (c)). The difference in radiation hardness between MCS $MAPbI_3$ perovskite powder and flash-evaporated $MAPbI_3$ perovskite film samples can be explained in terms of the bonding strength in the $PbI_6$ framework. As previously reported [25], the Pb–I bonds in MCS $MAPbI_3$ perovskite powder are stronger and shorter than those in flash-evaporated $MAPbI_3$ perovskite films. This difference is consistent with our results in terms of peak position differences obtained in XRD, PL, and UV-Vis absorbance spectra (figure 3.11 for XRD, figure 3.5 (c) vs. figure 3.9 (e) for PL, and figure 3.5 (b) vs. figure 3.9 (d) for UV-Vis absorbance).

## 3.4 Conclusions

We investigated the radiation hardness of organic–inorganic halide $MAPbI_3$ perovskites synthesized via mechanochemical synthesis and flash evaporation by measuring their physical and optical properties before and after the 10-MeV proton irradiation at various doses. The MCS $MAPbI_3$ perovskite powder samples did not exhibit considerable changes in their physical properties after the proton irradiation, indicating their radiation tolerance. Conversely, flash-evaporated $MAPbI_3$ perovskite film samples exhibited noticeable changes after irradiation at high doses. The radiation hardness difference between perovskite synthesis methods can be explained

by the differences in the bonding strength of the $PbI_6$ frameworks in the irradiated perovskites. In particular, the Pb–I bonds in MCS $MAPbI_3$ perovskite powder are stronger than those in the flash-evaporated $MAPbI_3$ perovskite film. This study helps in expanding the scientific understanding of the radiation hardness of perovskite material and demonstrates the high radiation tolerance of MCS $MAPbI_3$ perovskite. Further study on an MCS $MAPbI_3$ perovskite powder that can be converted to a film without losing its properties will enhance the application potential of $MAPbI_3$ perovskite for devices in harsh radiative environments, such as space.

## References


1. Mahmood K, Swain BS, Kirmani AR, Amassian A. 2015 *J Mater Chem A.* **3** 9051-7.
2. Kim M, Kim G-H, Oh KS, Jo Y, Yoon H, Kim K-H, Lee H, Kim JY, Kim DS. 2017 *ACS Nano.* **11** 6057-64.
3. Niu T, et al. 2018 *Energy Environ Sci.* **11** 3358-66.
4. Jeong J, et al. 2021 *Nature.* **592** 381-5.
5. Tsai H, et al. 2018 *Adv Mater.* **30** 1704217.
6. Zhao B, et al. 2018 *Nat Photonics.* **12** 783-9.
7. Stylianakis MM, Maksudov T, Panagiotopoulos A, Kakavelakis G, Petridis K. 2019 *Materials.* **12** 859.

8. Liu Y, et al. 2018 *Nat Commun.* **9** 1-11.

9. Hwang B, Lee JS. 2019 *Adv Opt Mater.* **7** 1801356.

10. Hwang B, Park Y, Lee J-S. 2021 *J Mater Chem C.* **9** 110-6.

11. Senanayak SP, et al. 2017 *Sci Adv.* **3** e1601935.

12. Senanayak SP, et al. 2020 *Sci Adv.* **6** eaaz4948.

13. McMeekin DP, et al. 2016 *Science*. **351** 151-5.

14. Leveillee J, Katan C, Even J, Ghosh D, Nie W, Mohite AD, Tretiak S, Schleife A, Neukirch AJ. 2019 *Nano Lett.* **19** 8732-40.

15. Lang F, et al. 2016 *Adv Mater.* **28** 8726-31.

16. Miyazawa Y, Ikegami M, Chen H-W, Ohshima T, Imaizumi M, Hirose K, Miyasaka T. 2018 *IScience*. **2** 148-55.

17. Lang F, et al. 2020 *Joule.*

18. Lee J, et al. 2021 *Advanced Materials Technologies*. **6** 2001131.

19. Lee W, et al. 2020 *Sci Rep*. **10** 1-10.

20. Markvart T. 1990 *Journal of Materials Science: Materials in Electronics.* **1** 1-12.

21. Inguimbert C, Messenger S. 2012 *IEEE Trans Nucl Sci.* **59** 3117-25.

22. Tan D, García F. 2019 *Chem Soc Rev.* **48** 2274-92.

23. Palazon F, El Ajjouri Y, Bolink HJ. 2020 *Adv Energy Mater.* **10** 1902499.

24. Elseman A, Shalan A, Rashad M, Hassan A. 2017 *Mater Sci Semicond Process.* **66** 176-85.

25. López CA, et al. 2020 *Sci Rep*. **10** 1-11.

26. Jiang S, et al. 2016 *Angewandte Chemie.* **128** 6650-4.

27. Baikie T, Fang Y, Kadro JM, Schreyer M, Wei F, Mhaisalkar SG, Graetzel

M, White TJ. 2013 *J Mater Chem A.* **1** 5628-41.

28. Kanaya S, et al. 2019 *The Journal of Physical Chemistry Letters.* **10** 6990-5.
29. Guo X, McCleese C, Kolodziej C, Samia AC, Zhao Y, Burda C. 2016 *Dalton Trans.* **45** 3806-13.
30. Caputo M, et al. 2019 *Sci Rep.* **9** 1-11.
31. Ahrenkiel R. 1992 *Solid-State Electron.* **35** 239-50.
32. Connelly BC, Metcalfe GD, Shen H, Wraback M. 2010 *Appl Phys Lett.* **97** 251117.
33. Staub F, Hempel H, Hebig J-C, Mock J, Paetzold UW, Rau U, Unold T, Kirchartz T. 2016 *Phys Rev Appl.* **6** 044017.
34. Pham ND, Tiong VT, Chen P, Wang L, Wilson GJ, Bell J, Wang H. 2017 *J Mater Chem A.* **5** 5195-203.
35. James DR, Liu Y-S, De Mayo P, Ware WR. 1985 *Chem Phys Lett.* **120** 460-5.
36. Xu H, et al. 2016 *RSC Adv.* **6** 48851-7.
37. Muniz FTL, Miranda MAR, Morilla dos Santos C, Sasaki JM. 2016 *Acta Crystallographica Section A: Foundations and Advances.* **72** 385-90.
38. Prochowicz D, Franckevičius M, Cieślak A, Zakeeruddin SM, Grätzel M, Lewiński J. 2015 *J Mater Chem A.* **3** 20772-7.
39. Jodlowski AD, Yépez A, Luque R, Camacho L, de Miguel G. 2016 *Angew Chem Int Ed.* **55** 14972-7.
40. Segovia R, Qu G, Peng M, Sun X, Shi H, Gao B. 2018 *Nanoscale Res Lett.* **13** 1-8.

41. Chaudhary B, Koh TM, Febriansyah B, Bruno A, Mathews N, Mhaisalkar SG, Soci C. 2020 *Sci Rep.* **10** 1-11.
42. Duan H-S, Zhou H, Chen Q, Sun P, Luo S, Song T-B, Bob B, Yang Y. 2015 *Physical chemistry chemical physics.* **17** 112-6.
43. Yin W-J, Shi T, Yan Y. 2014 *Appl Phys Lett.* **104** 063903.
44. Claeys C, Simoen E. Radiation effects in advanced semiconductor materials and devices: Springer Science & Business Media; 2013.
45. Messenger S, Burke E, Summers G, Xapsos M, Walters R, Jackson E, Weaver BJIToNS. 1999. **46** 1595-602.
46. Ziegler JF, Biersack J, Littmark UJ, Pergamon Press, New York. 1985.
47. Shin J, et al. 2019 *Nanoscale.* **11** 13961-7.
48. Lang F, Shargaieva O, Brus VV, Neitzert HC, Rappich J, Nickel NH. 2018 *Adv Mater.* **30** 1702905.
49. Lang F, Jošt M, Bundesmann J, Denker A, Albrecht S, Landi G, Neitzert H-C, Rappich J, Nickel NH. 2019 *Energy Environ Sci.* **12** 1634-47.
50. Brus VV, et al. 2017 *Adv Electron Mater.* **3** 1600438.
51. Malinkiewicz O, Imaizumi M, Sapkota SB, Ohshima T, Öz S. 2020 *Emergent Materials.* **3** 9-14.
52. Shin J, et al. 2022 *Nanotechnology*, **33** 065706.

# Chapter 4. Summary

In this dissertation, I have dealt with the study on the effect of high energy proton beam irradiation on nanomaterials such as the $WSe_2$ of two-dimensional material and $MAPbI_3$ of metal halide perovskite.

First, I investigated the proton irradiation effect on ambipolar $WSe_2$ field effect transistors by analysing the electrical characteristics before and after the irradiation. Proton induced changes in electrical characteristics showed different trends according to the proton beam dose. In low dose conditions, a positive gate voltage was induced due to the “positive bulk trap” and in high dose condition, a negative gate voltage was induced due to the “negative interface trap state”.

Secondly, the proton radiation hardness on organic-inorganic hybrid halide perovskite were studied. $MAPbI_3$ perovskite were synthesized by two kinds of methods; flash evaporation and mechanochemical synthesis. The physicochemical characteristics of the synthesized perovskite were systematically measured before and after the high-energy proton beam irradiation. Effects of the proton beam irradiation, such as radiation hardness, depended on the synthesis method. This study will help expand the understanding of the effect of high energy proton beam irradiation and suggests the possibility of application in radiation applications.

# 국문 초록

## 고에너지 양성자 조사가 나노 물질(이차원 텅스텐 다이셀레나이드와 메틸암모늄 납 할라이드 페로브스카이트)에 미치는 영향

신지원

서울대학교 물리천문학부

트랜지스터나 태양 전지와 같은 전자 소자에 대한 양성자 빔 조사의 효과에 대한 연구는 크게 두 가지의 이점을 가지고 있습니다. 첫 번째는 양성자 빔을 통하여 소자의 전기적 또는 광학적 성능을 제어할 수 있다는 점입니다. 양성자 빔의 에너지에 따라, 고에너지의 양성자 빔을 사용하여 소자에 결함을 유도하여 전류 레벨을 조절하거나 저에너지의 양성자 빔을 사용하여 계층 구조 물질을 단층으로 박리시켜 광학적 특성을 크게 향상시킬 수 있습니다. 그러나 이러한 현상에 대한 메커니즘을 명확히 하기 위해서는 추가적인 연구가 필요합니다. 두번째는 우주와 같은 고방사선 환경에서 전자 소자의 활용 가능성을

탐색할 수 있다는 점입니다. 지난 6월, 누리호가 성공적으로 발사됨으로 한국은 독자적 발사체를 우주로 쏘아 올린 7번째 나라가 되었습니다. 누리호는 순수 국산 기술로 만들어진 우주 발사체라는 것에 있어 의미가 큽니다. 미래 우주 산업은 태양광 산업, 우주 관광산업, 관측 산업 등, 여러 가능성을 품고 있어 국내외 막론하고 큰 관심을 받고 있는 분야입니다. 이를 나타내듯이 지난 50년간 평균적으로 연간 100 여개의 인공위성이 발사된 것에 반해 최근에 급격한 우주 산업의 성장으로 2021년에는 1400개 이상의 위성이 발사되었습니다. 이에 따라 우주 환경에서 활용가능한 전자 소자에 대한 수요가 증가하고 있습니다. 이 때, 우주선을 구성하는 감마선, 전자, 중성자 등 다양한 요소 중에서 양성자가 매우 높은 비율을 차지하기 때문에 양성자에 대한 영향 연구가 매우 중요합니다. 제가 연구한 물질 중 하나인 유기-무기 할로겐화 납 페로브스카이트는 높은 전력 변환 효율을 가지고 있어 차세대 태양 전지 물질로 주목 받으며 많은 연구가 이루어지고 있으며 최근 실제 우주에서 시범 적용 단계에 이르렀습니다. 그러나 안정성 및 성능 면에서 최대 활용을 위하여 더 많은 연구가 필요합니다.

이러한 측면에서, 본 학위논문에서는 첫 번째로 전이 금속 칼코겐 화합물인 텅스텐 다이셀레나이드 기반의 전계 효과 트랜지스터를 제작, 해당 전자 소자에 양성자 빔이 미치는 영향을 전기적, 물리화학적 특성 변화를 통해 논하였습니다. 전이 금속 칼코겐 화합물은 높은 이동도, 높은 온/오프 전류비, 두께에 따라 변화하는 밴드갭 등의 전계

효과 트랜지스터로 활용되기 좋은 특성을 가져, 차세대 소자 물질로 각광받고 있는 물질입니다. 그 중 텅스텐 다이셀레나이드는 다른 전이 금속 칼코겐 화합물과는 차별적으로 두께에 따라 전자 소자의 캐리어 유형이 변화하는 독특한 특성을 가집니다. 본 학위 논문에서는 전자 축적 영역과 정공 축적 영역 모두에 대한 양성자 효과를 살펴보기 위하여 양극성 유형의 트랜지스터를 설계 및 제작하였습니다. 제작된 소자에 다양한 선량 조건에서 10 MeV의 고에너지 양성자 빔을 조사하고 조사 전 후의 전기적 및 물리화학적 특성을 체계적으로 비교하였습니다. 이 때, 물리화학적 특성은 측정한계 내에서 변하지 않았으나 전류 레벨, 문턱전압 등의 전기적 특성은 조사 선량에 따라 변화하였습니다. 이러한 변화는 양성자 조사 유도 트랩(양성 벌크 트랩 및 음성 계면 트랩 상태)으로 설명되었습니다.

두 번째로, 유기-무기 할로겐화 납 페로브스카이트를 두 가지 방법으로 합성한 후 합성법에 따른 양성자 빔에 대한 경도를 논하고자 합니다. 이 때 사용된 합성법은 기계 화학 합성법과 순간 증발 합성법이며 두 방법 모두 건식 합성법이기 때문에 대표적인 페로브스카이트 합성법 중 하나인 스핀 코팅 기법에 비해 독성이 적다는 장점이 있습니다. 합성된 물질은 다양한 조사 선량의 고에너지 양성자 빔에 노출되었으며, 순간 증발 합성법과 달리 기계 화학 합성법은 높은 조사 선량에서도 물리 화학적 성질이 크게 변화하지 않았습니다. 이는 기계 화학 합성법으로 얻어진 페로브스카이트가 더 적은 격자 결함을

가지고 있어 물질 내 결합력이 더 강하기 때문으로 설명되었습니다.

**주요어 : 양성자 빔, 고에너지 방사선, 전이금속 칼코겐 화합물, 유무기 페로브스카이트**

**학번: 2016-20297**

## Publication Lists (First Authors)

1. Jiwon Shin, Kyungjune Cho, Tae-Young Kim, Jinsu Pak, Jae-Keun Kim, Woocheol Lee, Jaeyoung Kim, Seungjun Chung, Woong-Ki Hong and Takhee Lee, "Dose-dependent effect of proton irradiation on electrical properties of WSe2 ambipolar field effect transistors", Nanoscale, 11, 13961 (2019).
2. Jiwon Shin, Kyeong-Yoon Baek, Jonghoon Lee, Woocheol Lee, Jaeyoung Kim, Juntae Jang, Jaehyoung Park, Keehoon Kang*, Kyungjune Cho*, and Takhee Lee*, "Proton irradiation effects on mechanochemically synthesized and flash-evaporated hybrid organic-inorganic lead halide perovskites", Nanotechnology, 33, 065706 (2022).

## Publication Lists (Co-authors)

1. Jae-Keun Kim, Younggul Song, Tae-Young Kim, Kyungjune Cho, Jinsu Pak, Barbara Yuri Choi, Jiwon Shin, Seungjun Chung, and Takhee Lee, "Analysis of noise generation and electric conduction at grain boundaries in CVD-grown MoS2 field effect transistors", Nanotechnology, 28, 47LT01 (2017).
2. Kyungjune Cho, Jinsu Pak, Jae-Keun Kim, Keehoon Kang, Tae-Young Kim, Jiwon Shin, Barbara Yuri Choi, Seungjun Chung and Takhee Lee, "Contact-Engineered Electrical Properties of MoS2 Field-Effect Transistors via Selectively Deposited Thiol-Molecules", Advanced Materials, 30, 1705540 (2018).

3. Jinsu Pak, Yeonsik Jang, Junghwan Byun, Kyungjune Cho, Tae-Young Kim, Jae-Keun Kim, Barbara Yuri Choi, Jiwon Shin, Yongtaek Hong, Seungjun Chung, Takhee Lee, "Two-Dimensional Thickness-Dependent Avalanche Breakdown Phenomena in MoS2 Field Effect Transistors under High Electric Fields", ACS Nano, 12, 7109 (2018).
4. Barbara Yuri Choi, Kyungjune Cho, Jinsu Pak, Tae-Young Kim, Jae-Keun Kim, Jiwon Shin, Junseok Seo, Seungjun Chung, and Takhee Lee, "Effects of Electron Beam Irradiation and Thiol Molecule Treatment on the Properties of MoS2 Field Effect Transistors", Journal of the Korean Physical Society, 72, 1203, (2018).
5. Jinsu Pak, Kyungjune Cho, Jae-Keun Kim, Yeonsik Jang, Jiwon Shin, Jaeyoung Kim, Junseok Seo, Seungjun Chung, and Takhee Lee, "Trapped charge modulation at the MoS2/SiO2 interface by lateral electric field in MoS2 field-effect transistors", Nano Futures, 3, 011002 (2019).
6. Junseok Seo, Kyungjune Cho, Woocheol Lee, Jiwon Shin, Jae-Keun Kim, Jaeyoung Kim, Jinsu Pak and Takhee Lee, "Effect of Facile p-Doping on Electrical and Optoelectronic Characteristics of Ambipolar WSe2 Field-Effect Transistors", Nanoscale Research Letters, 14:313 (2019).
7. Jae-Keun Kim, Kyungjune Cho, Juntae Jang, Kyeong-Yoon Baek, Jehyun Kim, Junseok Seo, Minwoo Song, Jiwon Shin, Jaeyoung Kim, Stuart S. P. Parkin, Jung-Hoon Lee, Keehoon Kang, and Takhee Lee, "Molecular Dopant-dependent Charge Transport in Surface-charge-transfer-doped WSe2 Field Effect Transistors", Advanced Materials, 33, 2101598 (2021).
8. Jonghoon Lee, Woocheol Lee, Jeongjae Lee, Kyeong-Yoon Baek, Jiwon

Shin, Jae-Keun Kim, Junwoo Kim, Heebeom Ahn, Keehoon Kang & Takhee Lee, "Tailored Design-of-Experiments Approach for Device Performance Prediction and Optimization of Flash-Evaporated Organic Inorganic Halide Perovskite-based Photodetectors", Advanced Materials Technologies, 6, 2001131 (2021).

9. Inho Jeong, Kyungjune Cho, Seobin Yun, Jiwon Shin, Jaeyoung Kim, Gyu Tae Kim*, Takhee Lee*, and Seungjun Chung*, "Tailoring the Electrical Characteristics of MoS2 FETs through Controllable Surface Charge Transfer Doping Using Selective Inkjet Printing", ACS Nano,16, 6215 (2022).
10. Jaeyoung Kim, Kyungjune Cho, Jinsu Pak, Woocheol Lee, Junseok Seo, Jae-Keun Kim, Jiwon Shin, Juntae Jang, Kyeong-Yoon Baek, Jonghoon Lee, Seungjun Chung, Keehoon Kang, and Takhee Lee, “Channel-Length-Modulated Avalanche Multiplication in Ambipolar WSe2 Field-Effect-Transistors”, ACS Nano, 16, 5376 (2022)
11. Changjun Lee, Junwoo Kim, Jonghoon Lee, Woocheol Lee, Minwoo Song, Kyeong-Yoon Baek, Jiwon Shin, Jongwoo Nam, Jeongjae Lee, Keehoon Kang, and Takhee Lee, "Photo-Responsive Molecular Junctions Activated by Perovskite/Graphene Heterostructure Electrode", Advanced Optical Materials, in press (2022)
12. Heebeom Ahn, Keehoon Kang, Younggul Song, Woocheol Lee, Jae-Keun Kim, Junwoo Kim, Jonghoon Lee, Kyeong-Yoon Baek, Jiwon Shin, Hyungbin Lim, Yongjin Kim, Jae Sung Lee and Takhee Lee, "Resistive

Switching by Percolative Conducting Filaments in Organometal Perovskite Unipolar Memory Devices Analyzed Using Current Noise Spectra", Advanced Functional Materials, 32, 2107727 (2022).

13. Kyeong-Yoon Baek, Woocheol Lee, Jonghoon Lee, Jaeyoung Kim, Heebeom Ahn, Jae Il Kim, Junwoo Kim, Hyungbin Lim, Jiwon Shin, Yoon-Joo Ko, Hyeon-Dong Lee, Richard H. Friend, Tae-Woo Lee, Jeongjae Lee, Keehoon Kang, and Takhee Lee, "Mechanochemistry - driven engineering of 0D/3D heterostructure for designing highly luminescent Cs–Pb–Br perovskites", Nature Comm. accepted (2022)

## Presentations

1. Jiwon Shin et al "Proton irradiation hardness of organic−inorganic lead halide perovskites synthesized by mechanochemical synthesis and flash evaporation", 12th International Conference on Advanced Materials and Devices (ICAMD 2019), Jeju, Korea, Dec. 6-10, 2021.
2. Jiwon Shin et al "Proton Irradiation Effect on Organic−inorganic lead halide Perovskite Synthesized by Two Methods; Mechanochmical synthesized and Flash Evaporation", 2021 Fall Korean Physical Society Meeting (가을 한국물리학회), Virtual conference, Oct. 20-22, 2021. [Student oral talk]
3. Jiwon Shin et al “Proton Irradiation Effect on Mechanochmical synthesized Organic-inorganic lead halide Perovskite”, The 31st

International Conference on Molecular Electronics and Devices (IC ME&D 2021), Seoul, Korea, Jul. 8-9, 2021.

4. Jiwon Shin et al "Dose-dependent effect of proton beams on $WSe_2$ field effect transistors", NANO KOREA 2020, KINTEX, Korea, Jul. 1-3, 2020.
5. Jiwon Shin et al “Dose-Dependent Proton Beam Irradiation Effect on $WSe_2$ Ambipolar Field Effect Transistors”, Materials Research Society 2019 Fall Meeting (2019 MRS Fall Meeting), Boston, USA, Dec. 5, 2019.
6. Jiwon Shin et al "Dose-dependent proton beam irradiation effect on $WSe_2$-based ambipolar field effect transistors", The 30th International Conference on Molecular Electronics and Devices (IC ME&D 2019), Busan, Korea. May 9-10, 2019.
7. Jiwon Shin et al "Effect of Proton Irradiation on $WSe_2$ Ambipolar Field Effect Transistors", 26th Korean Conference on Semiconductor (한국반도체학술대회), Welihilli Park, Korea, Feb. 13-15, 2019. [Student oral talk]
8. Jiwon Shin et al "Effect of proton beam irradiation on $WSe_2$ ambipolar field effect transistors", the 29th International Conference on Molecular Electronics and Devices (IC-ME&D 2018), Kyungpook National University, Korea, May 10-11, 2018. [Best Poster Award]
9. Jiwon Shin et al "Proton Irradiation Effect on WSe2 Field Effect Transistors", 2018 Spring Korean Physical Society Meeting( 봄 한국물리학회), Daejeon, Apr. 25-27, 2018.